

DTIC FILE COPY

## REPORT DOCUMENTATION PAGE

AD-A227 371

Public reporting burden for this collection of information is estimated to average 1 hour per response, including gathering and maintaining the data needed, and completing and reviewing the collection of information. Send comments regarding this burden estimate or any other aspect of this collection of information, including suggestions for reducing this burden, to Washington Headquarters Services, Directorate for Information Operations and Reports, 1215 Jefferson Davis Highway, Suite 1204, Arlington, VA 22202-4302, and to the Office of Management and Budget, Paperwork Reduction Project (01-0401), Washington, DC 20503.

1. AGENCY USE ONLY (Leave blank)		2. REPORT DATE August 30, 1990		3. REPORT TYPE AND DATES COVERED Annual Report 1 July/89-30 June/90	
4. TITLE AND SUBTITLE Electrophoretic and Electrolytic Deposition of Ceramic Particles on Porous Substrates				5. FUNDING NUMBERS AFOSR-89-0474	
6. AUTHOR(S) L. Gal-Or, S. Haber, S. Liubovich					
7. PERFORMING ORGANIZATION NAME(S) AND ADDRESS(ES) Technion Research and Development Foundation Technion City, Haifa 32000, Israel				8. PERFORMING ORGANIZATION REPORT NUMBER AFOSR-TR 90-1047	
9. SPONSORING/MONITORING AGENCY NAME(S) AND ADDRESS(ES) -EOARD 223/231 Old Marylebone Rd. London NW1 5TH UK -AFOSR/NE, Dr. L. Schioler, Bolling AFB DC 20332-6448				10. SPONSORING/MONITORING AGENCY REPORT NUMBER 2306/A2	
11. SUPPLEMENTARY NOTES					
12a. DISTRIBUTION/AVAILABILITY STATEMENT Unlimited				12b. DISTRIBUTION CODE	
13. ABSTRACT (Maximum 200 words) Electrophoretic deposition of ceramic particles on porous graphite and their penetration into the pores was demonstrated and studied both theoretically and experimentally. The theoretical analysis enables to predict the penetration depth of the particles as function of two non-dimensional parameters based on solvent properties, field strength and particle size and concentration. In the experimental studies the amount of induced material was found to increase with the ratio of dielectric constant to viscosity of the solvent, as well as with particle concentration and field intensity. However, due to simultaneous buildup of an overlying deposit penetration as function of deposition time reaches a plateau. In parallel studies on electrolytic deposition, ZrO <sub>2</sub> coatings were deposited on porous graphite from an aqueous solution of ZrO(NO <sub>3</sub> ) <sub>2</sub> . The deposition kinetics and microstructure of the deposit were studied. The initial amorphous deposits transformed into crystalline ZrO <sub>2</sub> polymorphs with nanocrystalline dimensions following heat treatment.					
14. SUBJECT TERMS Electrophoresis, Ceramics, Penetration, Electrolytic Deposition, Zirconia				15. NUMBER OF PAGES	
				16. PRICE CODE	
17. SECURITY CLASSIFICATION OF REPORT Unclassified	18. SECURITY CLASSIFICATION OF THIS PAGE Unclassified	19. SECURITY CLASSIFICATION OF ABSTRACT Unclassified	20. LIMITATION OF ABSTRACT Unlimited		

NSN 7540-01-280-5500

Standard Form 298 (Rev. 2-89)  
Prescribed by ANSI Std. Z39-18

This document has been approved for public release and sale; its distribution is unlimited.

GAL-OR/ELECTROPH/TECH-42.TEV

Electrophoretic and Electrolytic Deposition of Ceramic  
Particles on Porous Substrates

L. Gal-Or, S. Haber, S. Liubovich

Summary of Annual Report

1 July/89 - 30 June/90

OR	
<input checked="checked" type="checkbox"/>	
<input type="checkbox"/>	
Location	
Distribution/	
Availability Codes	
Dist	And/or Special
A-1	



90 09 28 04±

# Electrophoretic and Electrolytic Deposition of Ceramic Particles on Porous Substrates

L. Gal-Or, S. Haber, S. Liubovich

Summary of Annual Report

1 July/89 - 30 June/90

## Introduction

The present phase of the research project concentrated on quantitative evaluation of the ceramic particles induced into the porous substrate as a function of deposition and solvent parameters. This evaluation was carried out both experimentally and theoretically based on an analytical model for deep electrophoretic penetration of particles into porous substrates. In parallel to the electrophoretic studies, the electrolytic deposition of ceramic coatings from aqueous solutions was studied from the electrochemical and microstructural aspects. The four enclosed manuscripts describe in detail the above mentioned studies. Following, therefore, is a concise description of the studies and their results.

## Experimental

The experimental studies were carried out on porous graphite substrates - UCAR Grade 45. This substrate has a 48% volume porosity with an average pore size of  $60\mu$ . The ceramic particles deposited and induced by electrophoresis were submicron colloidal  $\text{SiO}_2$  (Pyrogenic Aerosil) with a specific area of  $450 \text{ m}^2/\text{g}$ . The concentrations of the ceramic material in the solvent were 3, 13 and  $30 \text{ g/l}$ . The solvents in most experiments were water and isopropanol. For the study of the effect of solvent properties on penetration ethanol and pentanol were also used. The field intensity was varied between  $0\text{-}300\text{v/cm}$  and the deposition time between  $5\text{-}120 \text{ min}$ .

For quantitative determination of the impregnated  $\text{SiO}_2$ , the weight change of the specimen was recorded, after removal of the external deposit. The amount of induced  $\text{SiO}_2$  was also determined, in some cases, by weighing the residue after burn-off of the graphite at  $900^\circ\text{C}$  for 20 hrs.

The electrolytic deposition studies concentrated on the deposition of  $\text{ZrO}_2$  from a 0.1M  $\text{ZrO}(\text{NO}_3)_2 \cdot n\text{H}_2\text{O}$  aqueous solution. The deposits were obtained at current densities ranging from 15-100  $\text{mA}/\text{cm}^2$  and durations of 10-60 min. For kinetic studies the coating weights were determined with an accuracy of 0.05 mg. During deposition the variation of cell voltage, pH and temperature of the solution were measured.

The microstructure of the  $\text{ZrO}_2$  coatings was characterized by optical and scanning electron microscopy and the phase content was determined by X-ray diffraction. The microstructural studies were carried out on deposits that were fired at 400, 600 and 900°C for 1 hr.

### Theoretical

The theoretical analysis, at this stage, relates to a single particle travelling in a pore described as a long circular tube of mean pore diameter. Three driving mechanisms are considered: the hydrodynamic drag force exerted on the particle due to the electroosmotic flow of the solvent inside the pore, the electrophoretic force exerted on the particle and the stochastic Brownian force due to thermal fluctuations of the solvent molecules.

### Summary of Results

In addition to the formation of surface deposits, electrophoretic induction of ceramic particles into the porous substrate was demonstrated.

It was found that solvent properties such as the ratio between the dielectric constant and the viscosity ( $\epsilon/\eta$ ) have a significant effect on penetration. Thus the amount of induced  $\text{SiO}_2$  is ten times larger for water ( $\epsilon/\eta = 81$ ) than for pentanol ( $\epsilon/\eta = 420$ ). Penetration increases with particle concentration and with deposition time. However, a plateau is reached for the dependence of induced  $\text{SiO}_2$  on deposition time due to the build-up of an external coating. Thus the extent of penetration could be enhanced if the external deposit were constantly removed or prevented. An optimal field strength exists for particle penetration due to its dual effect. Increase in field strength increases the particle velocity but it also enhances the build-up of the external deposit which blocks penetration.

The theoretical analysis enables to predict the penetration depth of a ceramic particle inside the porous substrate under the influence of the electric potential gradient. It also enabled to derive the non-dimensional

parameters that affect the particle motion. It was thus deduced that the parameters which affect most the particle penetration are the Peclet number (Pe) and the deposition rate ( $\lambda$ ):

$$Pe = \frac{Ub}{D} = \frac{(U' + U'')b}{D}$$

$$\lambda = \frac{kb}{D}$$

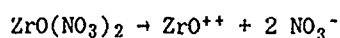
where:

- $U'$  - electrophoretic velocity
- $U''$  - electroosmotic velocity
- $b$  - pore mean radius
- $D$  - diffusion coefficient
- $k$  - local deposition rate

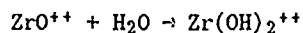
Large Peclet numbers and small deposition rates enhance penetration. Thus, deep penetration (over hundred pore diameters) can be achieved for very low deposition rates ( $\lambda < 0.1$ ) and for very high Peclet numbers ( $Pe > 100$ ). Deepest penetration is obtained for  $\lambda = 0$  which can be achieved if a repelling force between particles and pore walls would exist. Electroosmosis increases the Peclet number and thus penetration. The diffusion coefficient of the particle has a dual effect: its decrease increases the Peclet number, but it also increases the deposition rate. The theoretical analysis also indicates how the penetration can be controlled by selection of solvent properties, particle size and concentration and electric field strength.

The electrolytic deposition of  $ZrO_2$  is obtained through the following reactions:

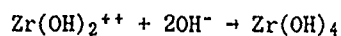
- a) dissociation of the zirconyl salt:



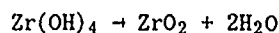
- b) hydrolysis of the zirconyl ion:



- c) interaction of the hydrated cation with  $OH^-$  ions generated at the cathode by reduction reactions described further on:



- d) dehydration of the hydroxide:



Several cathodic reactions are possible; however, the cathodic polarization curve indicates that the reduction of  $\text{NO}_3^-$  is the predominant  $\text{OH}^-$  producing reaction. The rate of deposit formation increases with current density the dependence reflecting the rate of  $\text{OH}^-$  generation. Faradaic efficiencies of 40-80% only were obtained attributable to reduction reactions that do not produce  $\text{OH}^-$  (such as reduction of  $\text{H}^+$ ) as well as to the formation of the hydroxide at sites removed from the substrate. Cell voltage and solution temperature increase as the coating process progresses. This is due to the formation of the deposit characterized by a high electric resistance.

The initial coating is a Zirconium hydroxide gel with an amorphous character. Microcracks develop in the coating during drying due to tensile stresses associated with non-uniform contraction. Firing of the coating led to its crystallization into fine, equiaxed submicron particles of monoclinic and tetragonal polymorphs of zirconia. Calculation of crystallite sizes by reflection broadening, indicated them to be 2 nm after treatment at 400°C and 12 nm when fired at 600°C for 1 hr. Under these conditions the polymorphs were undistinguishable. Firing for 1 hr at 900°C resulted in distinct crystallites of both phases, 20-25 nm in size. The volume fractions were 15% and 85% for the tetragonal and monoclinic phases respectively.

Future electrophoretic studies will include further optimization of penetration by inhibition of surface deposition. One approach will be the application of a low cathodic bias voltage to the specimen.

Following the derivation of optimal process conditions for penetration, experiments with lower expansion ceramics such as  $\text{HfTiO}_4$  will be performed.

Further studies on the electrolytic deposition will concentrate on prevention of cracking of the surface deposit during drying and study and optimization of in-pore deposition.

Electrophoretic Deposition and Deep Penetration  
of Ceramic Particles into Porous Substrates

L.Gal-Or, S. Liubovich, \*S.Haber  
Institute of Metals and Dept. of Mech. Eng.\*

Technion- Israel Inst. of Technology

### Abstract

The objective of the present study was to evaluate, experimentally, the feasibility of depositing ceramic particles on the surface of a porous substrate and inducing them into it by electrophoresis.

It was demonstrated that it is possible to charge and electrophoretically deposit both oxide (fused and colloidal  $\text{SiO}_2$ ) and non-oxide ( $\text{SiC}$  and  $\text{SiN}$ ) ceramics on a conductive graphite substrate. It was also shown that ceramic particles are induced into porous graphite and that under optimal conditions the whole cross-section of the specimens was penetrated.

The amount of induced material was found to increase with the ratio of dielectric constant to viscosity ( $\epsilon/\eta$ ) of the solvent as well as with particle concentration and field intensity. However, due to simultaneous build-up of an overlying deposit, penetration as function of deposition time reaches a plateau prior to filling of the whole pore volume.

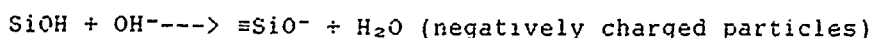


### Introduction

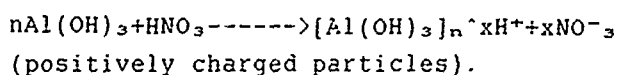
Electrophoretic deposition is obtained via migration of non-conductive but electrically charged particles, in an electric field towards one of the electrodes.

Two different charging modes are attributed to ceramic particles[1]:

a) a dissociation mode, such as dissociation of silanol groups present in silica:



b) an absorption mode, such as absorption of  $\text{H}^+$  from water or from weak acids:



Usually the polarity of the particles has to be determined experimentally as the charge is acquired spontaneously on mixing the particles with the solvent and it may be reversed upon addition of ionic compounds.

The surface charge, once formed, is then balanced by ions of an opposite charge derived from the solution and thus a double layer is formed around it.

According to the model proposed by Stern, this double layer consists of a rigid part with a linear potential gradient, and a diffuse part with a non-linear potential gradient termed "Zeta potential" (2).

When an electric field is applied to a charged particle the latter tends to migrate towards the electrode with the opposite charge. Its velocity however, is slowed down by the drag action of the surrounding double layer, which is pulled by the field in the opposite direction.

The mobility of the particle in an unbounded fluid is derived by equating the electric force with the frictional resistance and the relaxation force. Consequently, the mobility  $u$  is given by:

$$u = E \epsilon \zeta / 4\pi\eta [1 + f(kr)]$$

where:

$u$  - mobility

$E$  - field strength

$\epsilon$  - dielectric constant of fluid

$\zeta$  - Zeta potential of particles

$\eta$  - viscosity of fluid

$k$  -  $1/\text{double layer thickness}$

$r$  - radius of particle

$f(kr)$ , which varies between 0 and 1 for small and large values of  $kr$  respectively, represents the relaxation phenomenon, for  $k \ll r$ , the above expression reduces to the Smoluchowski equation, namely:

$$u = (E \times \epsilon \times \zeta) / 4\pi\eta$$

$u$  varies between 0 and  $20 \times 10^{-4}$  cm/sec/lv/cm.

The electrophoretic yield is given by:

$$y = a \int_0^t u E C S dt$$

where  $a$  - yield constant

$C$  - conc. of particles.

$S$  - area of electrode

$t$  - time

In the above equations it is assumed that the contribution of the hydrodynamic velocity to deposition is negligible its role being confined to maintenance of the suspension.

As for the phenomena that take place at the electrode, once the particles reach it, three possibilities are considered.

One hypothesis is that the particles undergo an electrode reaction which neutralizes them; this, however, does not account for the fact that deposits were obtained on a polymeric diaphragm located between two electrodes [4].

The second hypothesis states that the particles are brought to the electrode by a field which exerts sufficient force to overcome their mutual repulsion, thus allowing them to come close enough for the London-Van der Waals forces of attraction to predominate [5]. According to the Verwey & Overbeek [5], the minimal field strength necessary for this purpose (calculated from the energy of particles interaction) is:

$$E = 2F/3\epsilon\zeta r$$

A third hypothesis assumes that secondary processes taking place at the electrode can produce ions which coagulate the particles by discharging them, or produce hydroxides which polymerize and adsorb on particles, thus holding them together [6].

In the previous discussion the assumption was that the particle is suspended in an unbounded fluid. When electrophoresis in porous structures is considered, the presence of rigid boundaries affects both the electric field and the velocity of the particles.

According to J. Anderson(7, 8, 9) the effect of the pore wall on particle velocity is threefold:

- The applied electric field exerts a force on the d.l. at the pore wall if the latter is charged; electroosmotic flow or the fluid is thus produced, which either augments or opposes the electrophoretic velocity of the particle, depending on the polarity of  $\zeta_p$  vs  $\zeta_w$ .
- The pore wall distorts the electric flux around the particle, thereby intensifying the local electric field so that particle velocity is augmented.
- The pore wall creates additional viscous stresses in the fluid which slow down the particle.

A more detailed analysis of electrophoretic penetration is given in another report on this study (10).

Parameters which affect electrophoretic deposition and penetration are:

- Zeta potential of the particles
- Particle size
- Particle concentration
- Dielectric constant and viscosity of solvent
- Electric field strength.
- Time

In this work the feasibility of electrophoretic deposition of several kinds of ceramic particles was first evaluated, after which the effect of several deposition parameters on the amount of colloidal  $\text{SiO}_2$  induced into the pores of the substrate was studied.

#### Experimental Procedure

The deposition and impregnation experiments were carried out on porous graphite substrates.

The graphite was UCAR Grade 45, with 48% volume porosity and an average pore size of  $60\mu$ . Specimens of 20 x 20 x 7mm were mostly used. The ceramic powders deposited were:

- colloidal  $\text{SiO}_2$  - Pyrogenic Aerosil, submicron with a specific area of  $450 \text{ m}^2/\text{g}$
- fused  $\text{SiO}_2$  - 1-40 $\mu$
- SiC - <40 $\mu$
- SiN - 0.2-1.0 $\mu$

The ceramic particles were suspended in water, isopropanol, ethanol and pentanol.

The particle concentrations were 3, 13 and 30g/l.

Deposition was carried out at constant voltage with the current decreasing with time. Electric field strength was varied between 5 and 150 v/cm and deposition time between 5 and 120min.

Prior to deposition, specimens were rinsed with acetone for 5 min in an ultrasonic bath. After deposition they were dried in air for 24 hrs before examination. For quantitative determination of the impregnated material (colloidal  $\text{SiO}_2$  only) specimens were weighed before and after deposition to an accuracy of 0.1mg. In this case the external deposit was removed physically before weighing. As a cross check the amount of  $\text{SiO}_2$  induced into the porous structure was determined by weighing the residue after burn-off of the graphite at 950°C for 20hrs.

The specimens were examined by optical and electron microscopy both on the surface and in crosssection. The crosssections were obtained by fracturing the specimen after removal of the external deposit.

## RESULTS

A macroscopic view of deposits of SiC, SiN and fused  $\text{SiO}_2$  is seen in Fig. 2. The deposits are in a "green" state(unsintered) and since no special precautions had been taken, the deposits cracked during drying. The colloidal  $\text{SiO}_2$  formed a transparent deposit and is therefore presented at larger magnification in the SEM (fig 3 ). which shows a fluffy feather-like substance.

The presence of colloidal  $\text{SiO}_2$  in the pores of the graphite was demonstrated by examining the crosssection of a specimen by SEM (fig.4) and mapping the Si (fig 5) on the same area. Clusters of colloidal  $\text{SiO}_2$  are seen inside the crosssection, the distribution of elemental Si coinciding with the clusters.

Fig 6 shows the skeleton of  $\text{SiO}_2$  which remained after burn-off of the graphite at 900°C for 2 hrs. Presence of the  $\text{SiO}_2$  in the crosssection of the skeleton is seen in fig. 7.

Quantitative data of the penetrated  $\text{SiO}_2$  as function of solvent properties and deposition parameters, are given in Figs. 8-11. The amount of  $\text{SiO}_2$  is expressed as weight percent of the specimen.

The amount of penetrated  $\text{SiO}_2$  as function of the ratio between dielectric constant and viscosity of the solvent is shown in Fig. 8 for constant field,  $\text{SiO}_2$  concentration in solvent and deposition time. A strong influence of the solvent properties is revealed.

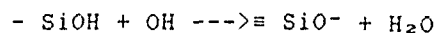
The dependence on the field intensity for three different  $\text{SiO}_2$  concentrations in water and for two concentrations in propanol is given in Fig. 9. To each concentration, there corresponds an optimal field. The  $\text{SiO}_2$  concentration in the solvent affects the amount of penetrated  $\text{SiO}_2$  for otherwise identical conditions: this is seen in Fig. 10 for deposition from water and from propanol.

The effect of deposition time on the amount of penetrated  $\text{SiO}_2$  is shown in Fig. 11 again for deposition from water and from propanol.

### Discussion

The feasibility of depositing oxide and non-oxide ceramics on an electrically conductive substrate by electrophoresis is demonstrated in Fig. 1.

Charging of the  $\text{SiO}_2$  particles is probably the consequence of dissociation of silanol groups in the silica:



The charge, thus obtained, is negative and in fact the particles migrate towards the anode in the electric circuit. Charging of non-oxide ceramics takes place probably via an absorption mechanism, with  $\text{SiC}$  acquiring a negative charge and depositing on the anode and  $\text{SiN}$  acquiring a positive charge and depositing on the cathode.

The cracks in the coating formed during drying as a result of shrinkage. A study is currently under way to modify the drying procedure, so that contraction stresses will be minimized and cracking prevented.

In order to verify the possibility of induction of ceramic particles into the pores, crosssections of coated graphite were prepared by fracturing the specimens. The presence of  $\text{SiO}_2$  clusters in the crosssection is evidenced both morphologically in fig 3. and by microanalysis in fig 4. The clusters vary in size possibly reflecting the variation of pore size. The distribution of elemental Si coincides as expected, with cluster locations.

A most interesting result was obtained during quantitative determination of the impregnated  $\text{SiO}_2$ . It was found that in specimens in which the induced  $\text{SiO}_2$  was at the higher levels (such as 0.6-2.5%) a  $\text{SiO}_2$  skeleton of the same shape and dimensions as the original specimen remained after removal of the graphite.

Moreover, the presence of the  $\text{SiO}_2$  throughout the crosssection of the skeleton indicates impregnation of the whole crosssection of the specimen.

The effect of solvent properties on penetration can be predicted from the theoretical analysis in (10). Penetration is enhanced at large Peclet numbers:

$$\text{Pe} = \frac{U b}{D}$$

where U is the particle velocity, b the mean pore

radius and D the diffusion coefficient of the particle. The electrophoretic velocity is proportional to  $\epsilon/\eta$  of the solvent. Four solvents were tested with  $\epsilon/\eta$  ratios ranging from 4.2 for pentanol to 81 for water. As predicted, the amount of penetrated  $\text{SiO}_2$  increased with this ratio (fig 7).

The electric field has a dual effect on the extent of particle penetration. Due to increase of the particle velocity and Peclet number with field strength, penetration is enhanced by it. However, the field enhances also the build-up of an external deposit on the substrate which blocks penetration. Therefore, there exists an optimal field strength (fig. 8), its value decreasing with increased particle concentration, because of faster build-up of the external coating at higher concentrations.

Penetration increases with particle concentration both in water and propanol. At low field strengths (5V/cm) the relationship is linear for the range of concentrations studied (fig.9).

Penetration increases with deposition time but reaches a plateau after a period which depends on solvent concentration and field strength. The fact that the plateau is reached before full impregnation of the pores, is probably due to the blockage by the external coating. Thus the extent of penetration could be increased if a way is found to prevent surface deposition.

### Conclusions

A variety of ceramic materials, both oxides and nonoxides, were deposited electrophoretically on a porous graphite substrate.

In addition to formation of surface deposits, electrophoretic induction of ceramic particles into the porous substrate was demonstrated.



Quantitative studies of the amount of penetrated material as function of deposition parameters, were carried out for colloidal  $\text{SiO}_2$ . It was shown that penetration is enhanced by a high dielectric constant and low viscosity of the solvent, by particle concentration and by field strength. Due to simultaneous build-up of an external deposit, a plateau is reached in the extent of penetration as function of time, prior to filling of the whole pore volume. Prevention or inhibition of surface deposition would favor an increased extent of penetration.

However, at the optimal conditions reached so far, penetration of the whole crosssection of the specimens was demonstrated.

#### Acknowledgement

Research sponsored by the Air Force Office of Scientific Research, Air Force Systems Command, U.S.A.F., under Grant No AFOSR 89-0474. The U.S. Government is authorized to reproduce and distribute reprints for Governmental purposes, notwithstanding any copyright notation thereon.

Bibliography

1. J. Davies, J. Coll. Interf. Sci. 63(3) 480,1978.
2. Y. S. Moya, Ceramic Bull, 59 (12),1980.
3. O.M. Bockris, K. N. Reddy, "Modern Electrochemistry"  
Vol. I,1970.
4. D.R. Brown, F.W. Salt, J. Appl. Chem. 15, 40, 1965.
5. E. J. W. Verwey, J. Th. Overbeek, "Theory of the Stability of  
Lyophobic Colloids" 1948, Elsevier.
6. P. Benson Electocim Acta, 9,275 (1964).
7. J. L. Anderson, Proc. Electrochem. Soc., 1985p. 103.
8. H.Y. Keh, J.L. Anderson, J. Fluid Mech. 153, 417 (1985).
9. J.L. Anderson, J. Colloid. Interf. Sci. 105 (11) 45 (1985).
10. S. Haber, L. Gal-Or, "Electrophoretic Deposition and Deep  
Penetration of Ceramic Particles Inside Porous Substrates  
Analytical Model", submitted.

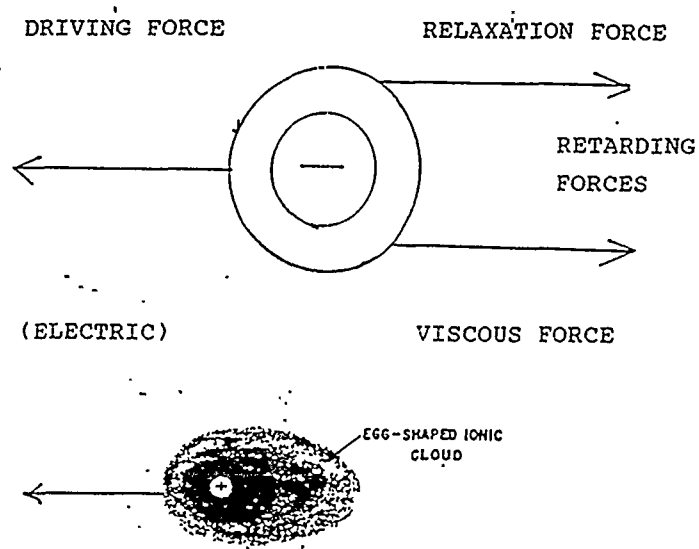


Fig.1 Egg-shaped ionic cloud and forces acting on a moving particle

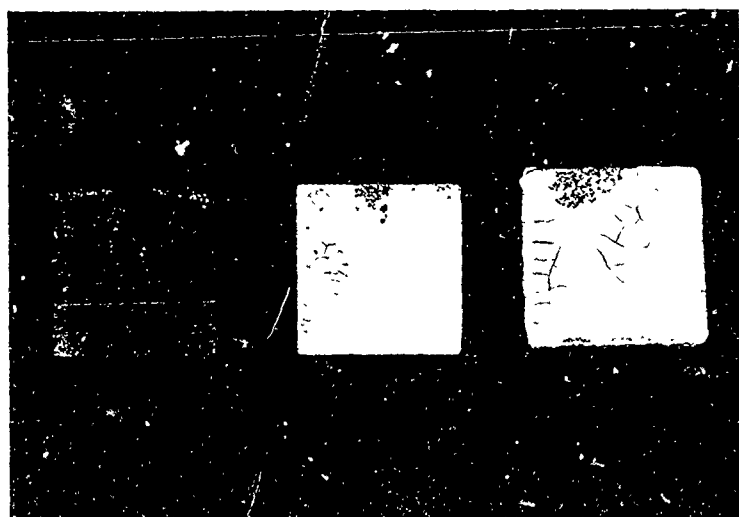


Fig.2 "Green" deposits of  $\text{SiC}$ ,  $\text{SiN}$  and fused  $\text{SiO}_2$  (from left to right) on graphite.

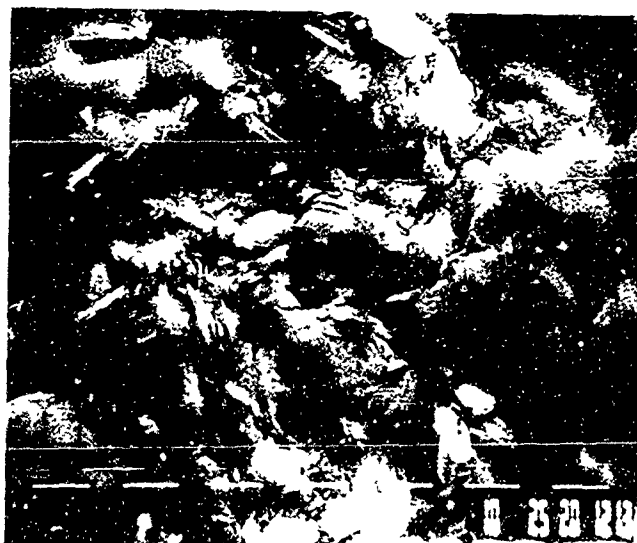


Fig.3 Colloidal  $\text{SiO}_2$  deposit on graphite



Fig.4 Colloidal  $\text{SiO}_2$  clusters inside the porous graphite (view of a crosssection).

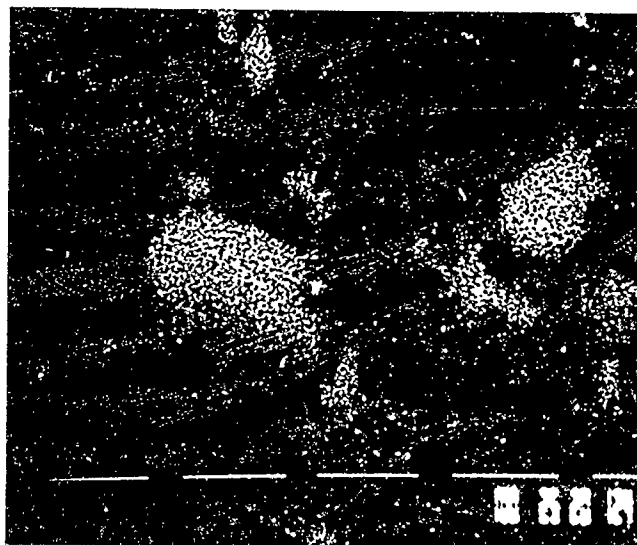


Fig.5 X - ray mapping for Si on area seen in Fig. 4

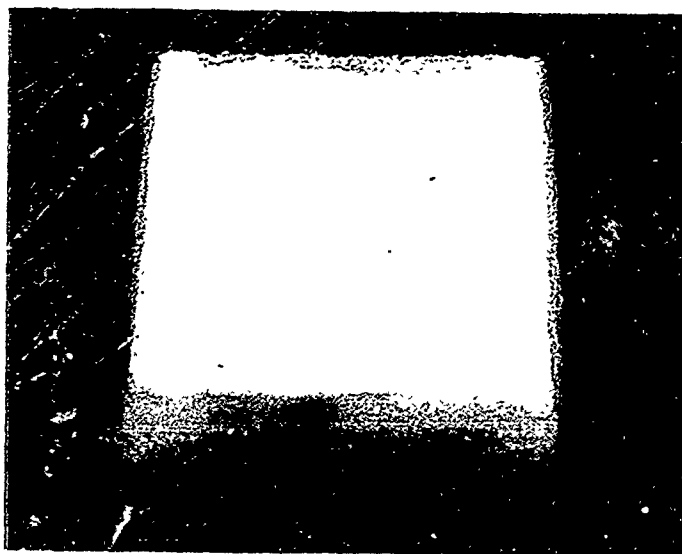


Fig.6  $\text{SiO}_2$  skeleton that remained after graphite burn-off

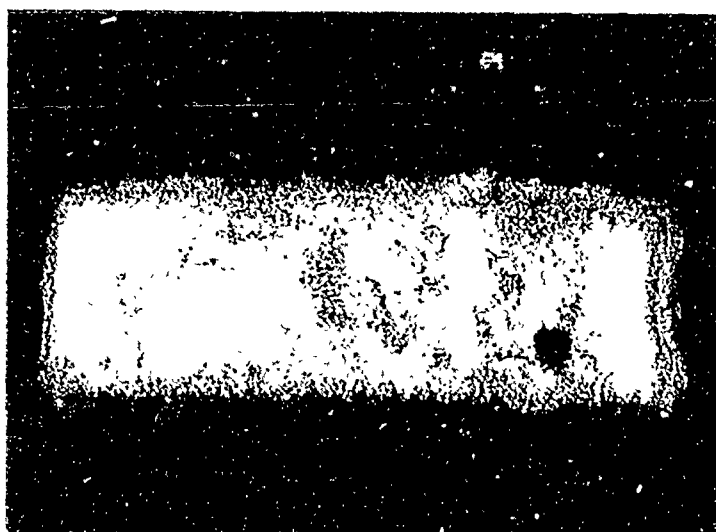


Fig.7 Crossection of skeleton seen in fig.6

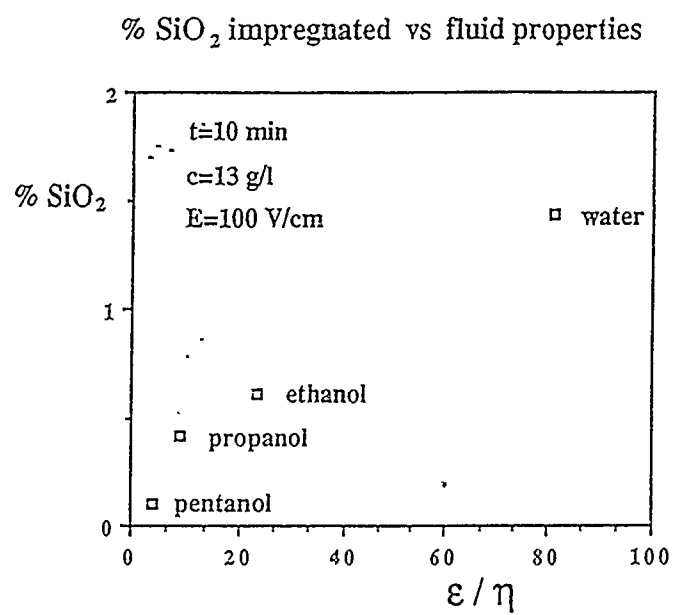


Fig.8 Amount of SiO<sub>2</sub> that penetrated the porous graphite from various solvents.



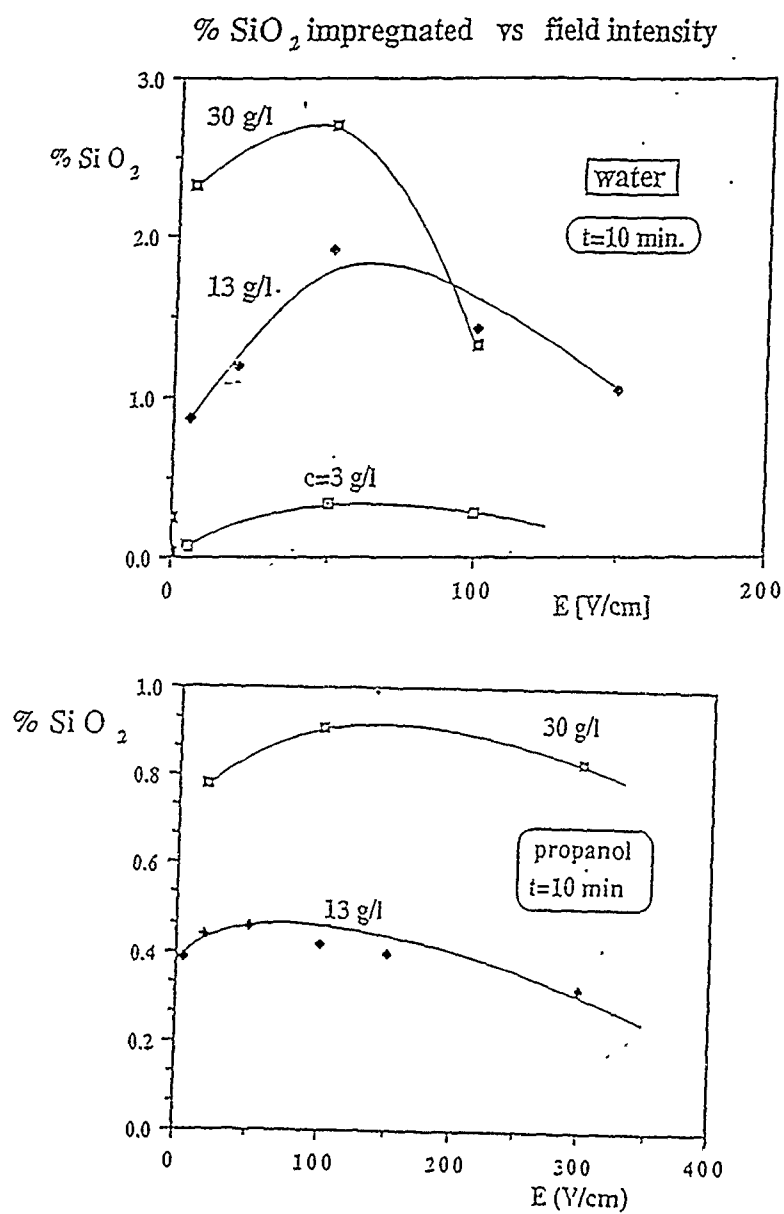


Fig.9 Amount of penetrated SiO<sub>2</sub> as function of electric field intensity.

% SiO<sub>2</sub> impregnated vs SiO<sub>2</sub> concent.

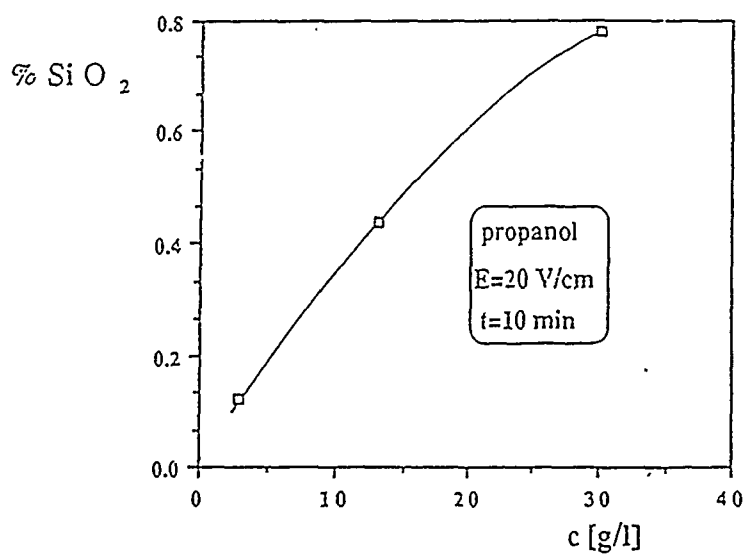
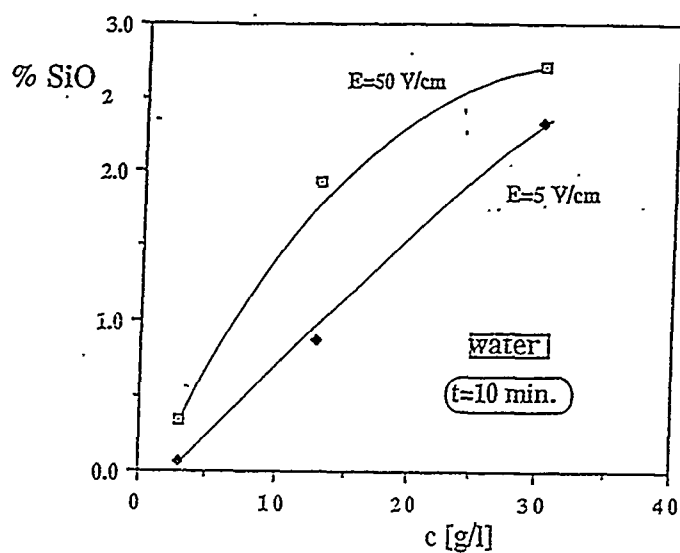


Fig.10 Amount of penetrated SiO<sub>2</sub> as function of its concentration in the solvent.

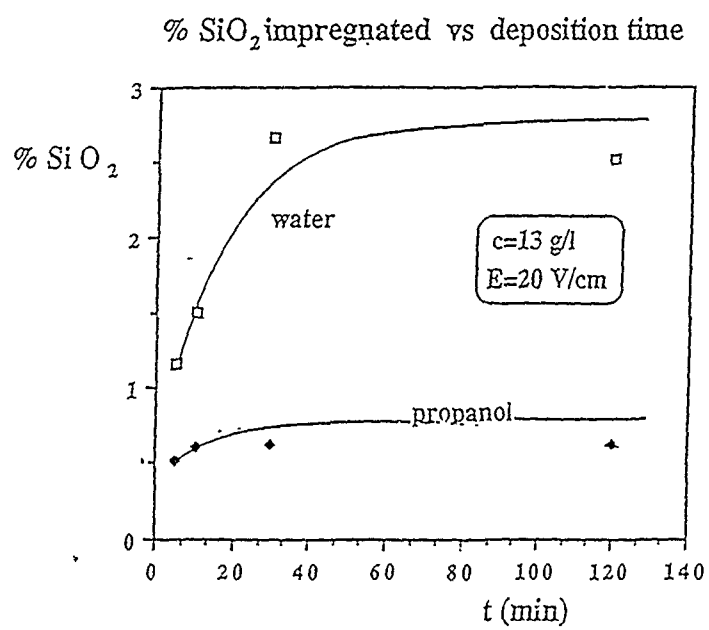


Fig.11 Effect of deposition time on amount of penetrated SiO<sub>2</sub>

An Analytical Model for  
Deep Electrophoretic Penetration and Deposition of  
Ceramic Particles Inside Porous Substrates.

by

S. Haber and L. Gal-Or

Dept. of Mech. Eng. and Institute of Metals  
Technion - Israel Inst. of Technology

1. ABSTRACT

The electrophoretic penetration of colloidal silica particles into a porous graphite substrate is investigated. The graphite substrate is immersed in a suspension containing the particles and positioned between two electrodes. An electric potential gradient between the graphite and the electrodes is used to drive the silica particles into the pores. Three driving mechanisms are identified: the hydrodynamic drag force exerted on the particles due to the electroosmotic flow of the solvent inside the pores, the electrophoretic force exerted on the particles and the stochastic Brownian force due to thermal fluctuations of the solvent molecules. While subjected to these forces, the particles may reach the walls of the pore and the short range van der Waals forces may cause their capturing and deposition onto the walls.

The objectives of this paper are: a) to predict the penetration depth of a single ceramic particle moving inside a porous substrate under the effect of an electric potential gradient, b) to derive the nondimensional parameters characterizing the motion of the ceramic particles, and c) to gain a physical insight on the various mechanisms governing penetration. Qualitatively, the results are that penetration depths are governed by a favorable (if large) Peclet number and unfavorable (if large) local deposition rate number. Quantitative results are also provided.

2. INTRODUCTION

Deep penetration and deposition of ceramic materials on oxidizable porous substrates has been a major concern of the aero-space industry. The extremely strong, light and sometimes porous composite of carbon-carbon may undergo undesired processes if

exposed to a high temperature oxidizing environment. Chemical Vapor Deposition (CVD) of ~~inert~~ silica, silicon-carbide etc. onto the walls of the pores, has been suggested in the past (1-2) to protect the composite from deterioration. Alas, CVD has proven to be extremely slow and only shallow penetration has been detected. A rather new method to protect porous substrates by electrophoresis is studied and described in detail in part II. In essence, an electric potential gradient is used to drive colloidal particles deep into the voids of a porous model material for carbon-carbon - porous graphite. The purpose of this paper (Part I) is: a) to provide an overview of the existing theory and mathematical models closely related to Deep Electrophoretic Deposition (DED), b) to suggest a theory and a mathematical model by which DED can be analyzed and the non-dimensional parameters governing the process be obtained, and c) to predict penetration depths for a given set of parameters.

The motion of a single particle under the effect of electrophoretic forces has first been addressed by Smoluchowski (1918) and subsequently by many others (3-15). Smoluchowski predicted that a rigid spherical particle possessing an electric double layer and embedded in an unbounded flow field would be forced to move if subjected to an electrical potential gradient. The mobility of the particle depends linearly upon the dielectric constant of the fluid, the potential gradient, the zeta potential of the particle and is inversely proportional to the fluid viscosity. Wall effects were accounted for by Morrison & Stukel (1970) and Keh & Anderson (1985) for the case of a particle travelling in close proximity to the containing boundaries of the flow field. Keh & Anderson (1985) have shown that (if electroosmosis is disregarded) the particle would experience an increasing drag force and reduced mobility. It was also shown, that due to the electric field, the insulating rigid walls would induce an electroosmotic flow, its direction depending on the sign of the wall zeta potential. Thus, a neutral particle immersed in the fluid would be dragged by the electroosmotic flow and move with almost identical velocity. In case the particle is also subjected to an electrophoretic force, the particle would move with the combined electrophoretic and electroosmotic velocities. Superimposition is allowed due to the linearity of the governing low Reynolds number flow field equations. In addition, a sub-micron particle would experience an erratic Brownian motion due to the thermal fluctuations of the fluid molecules. Consequently, deterministic evaluation of the particle path under the combined effects of electroosmosis, electrophoresis and Brownian motion is invalid and a probabilistic approach must be adopted (van-Kampen (1983)).

The fluid motion inside a porous substrate under the effect of a *pressure gradient* (known as Darcy's law) has been addressed by many investigators. To devise the micro-pattern of the flow field, unit cell models (19-21) as well as more advanced finite elements approaches for spatially periodic structures (22-27) were applied. However, no equivalent treatment exists for the case of electroosmotic flow through a porous structure, namely, the flow generated under the effect of an electric potential gradient. Since, a particle would be dragged by this interstitial electroosmotic flow, its evaluation is of foremost significance if one desires to calculate mean penetration depths of the ceramic particles. A general approach in which we modify Darcy's law so that it would incorporate electroosmotic effects is addressed in a separate paper (Haber (1990)).

The second effect to be accounted for is the direct electrophoretic force exerted on a particle travelling inside the small pores. Numerous treatments exist for the motion of a small rigid particle at low Reynolds numbers, wall effects excluded (29) and included (29-32). The fine structure of a porous substrate enveloping a particle was treated in various ways, for instance, a spherical particle travelling along an infinitely long cylinder of circular cross-section, a spherical particle embedded in a flow field which is bounded by a spherical envelope with pre-assumed free surface (or free vorticity) boundary conditions, and a small spherical particle moving inside a spatially-periodic lattice of pre-arranged large spherical particles. Notwithstanding, all of the previous models assumed *no-slip* boundary conditions over the particle surface, whereas the electrophoretic force is applied via a unique *slip* boundary condition. Thus, the known approaches must be rectified accordingly.

The third effect, the random Brownian force due to the thermal fluctuations of the fluid, was treated by two different methods in the past. The first method applies a Lagrangian viewpoint of the problem utilizing Langevin's equation to evaluate mean particle velocity and dispersion (33,34). The second method applies an Eulerian approach where a Fokker-Planck equation is formulated and a moment method developed by Taylor-Aris is utilized to derive the pertinent means (35-37). Generally, it is accepted (and for linear cases can be proven (18)) that these methods would yield identical results and the choice between the methods is a matter of convenience.

In the next chapter we shall address the three foregoing mechanisms where we provide: a) a short recapitulation of the basic equations governing electroosmotic flow in porous structures derived elsewhere (Haber 1990), b) a model for the motion of a particle

in a long cylindrical tube under the effect of an electric field, (a model simulating the motion of a particle in a porous structure), and c) a model for the stochastic behavior of the Brownian particle under the combined effect of electroosmosis and electrophoresis utilizing Fokker-Planck's equation.

### 3. METHOD OF SOLUTION

#### 3a. Electroosmosis in Porous Media

The flow through porous media generated by an electric potential gradient was analytically investigated by Kozak & Davis (1986, 1989) using a unit cell model and by Haber (1990) using a simple approach based on the known solution of the flow field through a long circular tube (in close similarity to one of the approaches used to analytically prove Darcy's law). Similar approaches for pressure driven flows were used to determine filtration efficiencies in porous substrates (39). We recapitulate here the basic assumptions and results presented by Haber (1990).

The governing field equations for the flow through a long circular tube induced by an electric potential gradient are based on Stokes' equations for low Reynolds number flows, i.e.

$$\eta \nabla^2 \mathbf{v} = \nabla p \quad \nabla \cdot \mathbf{v} = 0 \quad [1]$$

where  $\mathbf{v}$  and  $p$  are the velocity and pressure fields and  $\eta$  stands for the viscosity of the fluid. The boundary conditions which the velocity field satisfies over the cylinder walls are (17):

$$v_r = \frac{\epsilon \zeta_w}{4\pi\eta} \frac{\partial \phi}{\partial z}, \quad v_r = 0 \quad @ \quad r = b \quad [2]$$

where  $\epsilon$  is the dielectric constant of the fluid,  $\zeta_w$  is the zeta potential at the cylinder wall,  $\phi$  stands for the electric potential,  $b$  is the radius of the tube and  $(r, z)$  are polar coordinates, the  $z$  coordinate coinciding with the cylinder axis. It should be noted that the no-slip condition can no longer be applied and in its place we use condition [2].

The solution for  $v$  is easily derived for a fully developed flow, namely,  $\partial v_z / \partial z = 0$ . It is a simple superposition of the effects of the pressure gradient and the electric potential gradient. Integrating over the tube cross-section, the mean interstitial velocity is obtained:

$$\bar{v}_z = -\frac{b^2}{8\eta} \frac{\partial p}{\partial z} - \frac{\epsilon_p \epsilon_w}{4\pi\eta} \frac{\partial \phi}{\partial z} \quad [3]$$

Integrating over the entire cross-section of the porous medium the superficial velocity is,

$$v_z = -\frac{\epsilon_p \langle b^4 / b^2 \rangle}{8\eta} \frac{\partial p}{\partial z} - \frac{\epsilon_p \epsilon_w}{4\pi\eta} \frac{\partial \phi}{\partial z} \quad [4]$$

where  $\epsilon_p$  stands for the medium porosity.

Since a homogeneous porous medium contains pores in all possible directions, a similar procedure can be applied for pores oriented along the  $x$  and  $y$  directions. Expressions similar to [4] can be obtained for  $v_x$  and  $v_y$  and further generalized to derive the following expression for  $v$  in vectorial notation,

$$\mathbf{v} = -\Gamma \nabla p - \gamma \nabla \phi \quad [5]$$

where

$$\Gamma = \frac{\epsilon_p \langle b^4 / b^2 \rangle}{8\eta}, \quad \gamma = \frac{\epsilon_p \epsilon_w}{4\pi\eta} \quad [6]$$

Here  $\Gamma$  and  $\gamma$  can be viewed as the hydrodynamic and electric permeabilities, respectively. Equation [5] can be viewed as a generalization of Darcy's law for the case where an electrical potential gradient as well as a pressure gradient is imposed over a porous medium. It is obvious that these two forces are decoupled and a potential gradient alone can induce *electroosmotic* flow inside a porous structure. Increasing the electrical permeability,  $\gamma$ , would cause an increase in the electroosmotic flow. Thus, an increase in medium porosity, fluid dielectric constant and zeta- potential of the pore walls and decrease



in fluid viscosity would cause enhanced flow through a porous structure for a given potential gradient.

In addition, one must satisfy mass conservation which results in the following continuity equation for incompressible fluid,

$$\nabla \cdot \mathbf{v} = 0 \quad [7]$$

Equations [5] and [7] and the appropriate boundary conditions on  $\phi$  and  $p$  do not constitute a complete set by which the velocity, pressure and potential fields can be evaluated. An additional relation between the flux of the electric charge  $\mathbf{j}$  and the electric potential and pressure gradient can be established in a manner similar to the derivation of equation [5] :

$$\mathbf{j} = -\gamma \nabla p - K \nabla \phi \quad [8]$$

where  $K$  is the electric conductivity. It is interesting to note that  $\gamma$  appears both in [5] and [8] in full agreement with Onsager's reciprocal rule. The exact evaluation of  $K$  is of no interest at the moment and will not be addressed. Similar to [7] we obtain,

$$\nabla \cdot \mathbf{j} = 0 \quad [9]$$

which is simply Kirchoff's law applied to a porous medium.

Utilizing [5], [7], [8] and [9] it is easy to show that  $\phi$  and  $p$  can be decoupled and satisfy the following equations for a homogeneous medium:

$$\nabla^2 \phi = \nabla^2 p = 0 \quad [10]$$

i.e.  $\phi$  and  $p$  are harmonic functions which can easily be derived for a given set of boundary conditions.

For the very simple case of an infinite slab of thickness  $c$ , which is subjected to a potential drop  $\phi_2 - \phi_1$  and a zero pressure gradient (along, say, the  $z$  direction), the steady-state solutions for  $\phi$  and  $\mathbf{v}$  are simply

$$\phi = \phi_1 + (\phi_2 - \phi_1)z/c, \quad v = U' \equiv -\gamma(\phi_2 - \phi_1)/c. \quad [11]$$

Thus, the electroosmotic velocity through the slab is uniform and constant. We adopt the symbol  $U'$  for the velocity solution of this simple case and shall apply it later on in chapter 3c.

### 3b. Electrophoretic Motion of a Particle

The electrophoretic velocity  $U''$  of a small rigid spherical particle suspended in an *unbounded* flow field of viscosity  $\eta$  and subjected to an external electric potential gradient  $E = -\nabla\phi$  was first obtained by Smoluchowski,

$$U'' = -\frac{e\zeta_p}{4\pi\eta} \nabla\phi \quad [12]$$

where  $\zeta_p$  is the zeta potential over the particle interface. The basic assumptions made to derive [12] are that the Debye screening length is much smaller than the particle dimension and that the particle translates in an unbounded flow field.

If the particle translates at close proximity to a rigid surface, wall effects must be accounted for (e.g. Keh and Anderson(1985)). Notwithstanding, for particle dimensions which are more than ten times smaller than its distance to the wall, Smoluchowski's equation is an excellent approximation (given that no electroosmotic flow exists).

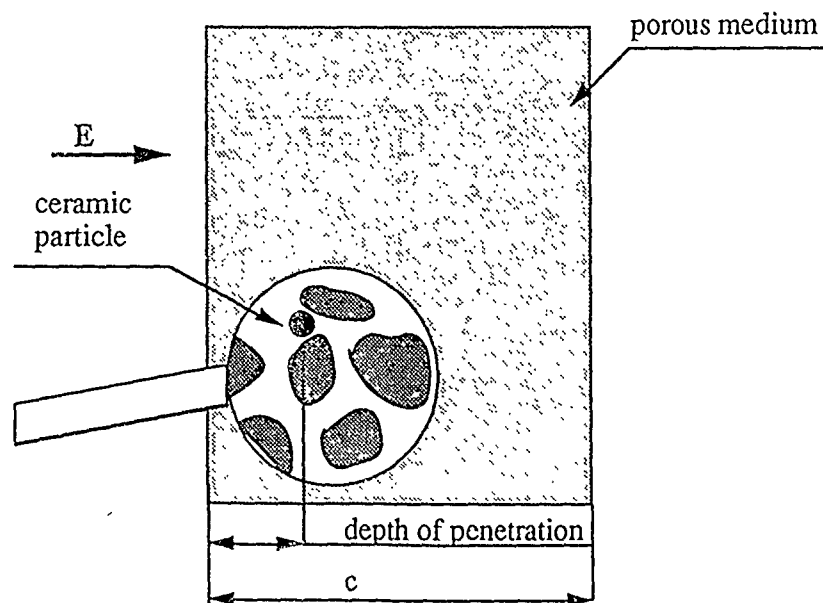
It is a well known result from the theory of low Reynolds number flows (40,41) that a particle approaching a rigid wall (subjected, for instance, to gravity forces) will experience a growing hydrodynamic resistance which at the limit of zero gap increases to infinity. However, the condition of slip velocity over the particle boundaries will cause that resistance to grow in a slower manner up till a gap of the order of the Debye screening length. An exact treatment of this hydrodynamically singular behavior awaits exploration. However, over these very small distances one has to consider other surface (e.g. London-van der Waals) forces which eventually lead to the attraction of the particle to the walls. Thus, it seems reasonable to assume that Smoluchowski's equation can be used as a first order approximation for the mobility of a particle over the entire range of particle-wall gaps.

Henceforth, we shall assume that equation [12] is applicable for the case of a single rigid particle immersed in a fluid of viscosity  $\eta$  and bounded by the walls of a long tube.

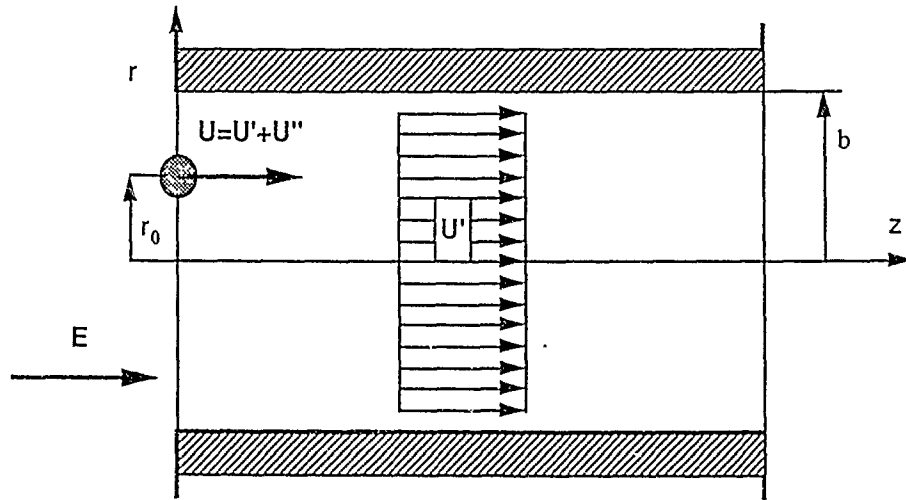
### 3c. The Probability Distribution for Particle Penetration Depths

#### 3c.1 Statement of The Problem

Small sub-micron particles travelling inside the pores of a porous substrate (see figure 1) are strongly affected by the thermal fluctuations of the fluid molecules and experience Brownian motion. This stochastic motion must be superimposed to the deterministic electrophoretic motion and electroosmotic induced velocity which are primarily parallel to the direction of the pore axis. The Brownian motion causes the particle to cross streamlines and sample all possible transverse positions which leads to the phenomenon known as Taylor dispersion.



Tracing down exactly the trajectory of a particle is therefore of no consequence. What we seek is the probability distribution that a particle entering the porous substrate would reach a given depth and not be deposited on the walls during its erratic motion inside the pores. In addition, the very complex and random structure of the porous substrate makes it impossible to obtain more than a formal representation of the equations and boundary conditions. The mathematical formulation must hinge on a simplified geometrical model for the porous structure which would be amenable to mathematical analysis. One of the very common approaches is to treat a single pore as a long circular tube of mean pore diameter its axis coplanar with the local superficial velocity direction. Such a model is handicapped by the fact that no pronounced *lateral* dispersion of the particles across the porous substrate is allowed. However, since only the mean *longitudinal* particle motion is sought such a model is expected to provide valid results on the main parameters affecting penetration depths. Figure 2 describes the basic geometrical and kinematical parameters applicable to the problem.



The general differential equations governing the problem is Fokker-Planck's equation for the probability distribution. In our case it assumes the form,

$$\frac{\partial p}{\partial t} + \nabla_z \cdot J_z + \nabla_r \cdot J_r + \nabla_\theta \cdot J_\theta = \frac{1}{r_0} \delta(z) \delta(r - r_0) \delta(\theta - \theta_0) \delta(t) \quad [13]$$

where

$$\begin{aligned} J_z &= Up - D_z \nabla_z p, & J_r &= -D_r \nabla_r p, & J_\theta &= -D_\theta \nabla_\theta p \\ D_z &= kTM_z, & D_r &= kTM_r, & D_\theta &= kTM_\theta \end{aligned} \quad [14]$$

$$U = U'(t) + U''(t)$$

Here  $p(r, z, \theta, t / r_0, 0, \theta_0)$  stands for the conditional probability that a particle initially located at  $(r_0, 0, \theta_0)$  reaches the infinitesimal volume around  $(r, z, \theta)$  after time  $t$ . The polar coordinate system  $(r, z, \theta)$  coincides with the pore axis where  $r$  stands for the radial distance from the pore axis,  $z$  is the distance measured along the pore axis from the pore entrance and  $\theta$  is the azimuthal angle. The symbol  $U$  stands for the deterministic part of the velocity of the particle, composed of its electrophoretic velocity and the electroosmotic velocity of the suspending field. It must be stressed that the interstitial flow due electroosmosis  $U''$  does not possess the commonly agreed upon parabolic (Poiseuille) form. It is very well approximated by plug flow (as shown in figure 2) for pore diameters larger than Debye's screening length (a condition normally met). Thus,  $U$  is a uniform function with respect to the spatial coordinates as long as the particle diameter is at least ten times smaller than the pore diameter. The flux  $J_z$  parallel to the axis of the pore depend on particle convection and diffusion along the pore axis, whereas the fluxes  $J_r$  and  $J_\theta$  arise from diffusion only. The diffusion coefficients  $D_z$ ,  $D_r$  and  $D_\theta$ , the first one parallel and the latter perpendicular to the pore axis, depend on the absolute temperature  $T$  of the liquid and the respective particle mobilities  $M_z$ ,  $M_r$  and  $M_\theta$ . This generalized Stokes-Einstein relationship provided in [14] accounts for wall effects through the anisotropic form of the mobility tensor. From the physical point of view, it is obvious that the particle would experience unequal hydrodynamic resistance to its motion perpendicular and parallel to the pore axis. The mobility tensor components were approximately evaluated in Happel and Brenner (1973). It is shown that, for particles of radius  $a$  small compared to their distance to the wall, the mobilities  $M_z$ ,  $M_r$  and  $M_\theta$  are approximately equal and possess the following form,

$$M_z \approx M_r \approx M_\theta \approx 1/(6\pi\eta a) \quad [15]$$

The boundary condition which must be satisfied by the probability distribution  $p$  is,

$$-D \frac{\partial p}{\partial r} = \kappa p \quad @ \quad r = b \quad [16]$$

where  $\kappa$  is the local deposition rate and  $b$  stands for the pore mean radius.

The left hand side of [16] represents the diffusional flux of probability towards the pore walls whereas the right hand side represents the probability that a particle located at close proximity to the walls would indeed be deposited. The numerical value of  $\kappa$  depends on particle shape and dimension, electrostatic and hydrodynamic forces and the physical properties of the materials comprising the particles, the porous substrate and the suspending liquid. Indeed, it is extremely difficult to obtain  $\kappa$  from first principles. A feasible method to attain this end would be to devise an experiment in which one would utilize the given materials of the ceramic particles, porous substrate and liquid.

### 3c.2 Analytical Solution and Results

It is very useful to state the non-dimensional parameters and time scales of the problem before we attempt to obtain an analytical or numerical solution of [13]. It is easy to show from [6] that the pertinent time scale within which steady electroosmotic flow can be established is,

$$\tau_M = \frac{c}{\gamma E} \quad [17]$$

where  $E$  is the externally applied electrical field.

Similarly, it can be shown from [13], [14] and [16] that three time scales exist for the penetration process of Brownian ceramic particles into the porous substrate. The first time scale is linked with the convective term of the Fokker-Planck equation, namely,

$$\tau_c = \frac{c}{U} \quad [18]$$

which determines the time it would take the particle to cross the porous slab.

The second time scale is related to the diffusive process, namely, the time it takes a Brownian particle to cross streamlines and sample all radial positions inside the tube,

$$\tau_D = \frac{b^2}{D} \quad [19]$$

The third time scale is obtained from boundary condition [16] and determines the deposition rate, namely,

$$\tau_R = \frac{b}{K} \quad [20]$$

If we assume that the Brownian particles were introduced into the solution after electroosmotic steady state flow has been established, ( $U$  is time independent) non-dimensionalization of the Fokker-Planck equation and the associated boundary conditions results in two non-dimensional parameters which determine the solution completely. The first parameter can be identified as the Peclet number of the problem,

$$Pe = \frac{Ub}{D} = \frac{(U' + U'')b}{D} \quad [21]$$

which determines the relative significance of the convective process vis-a-vis the diffusive process.

The second nondimensional parameter, henceforth called as the deposition rate parameter, determines the ratio between the diffusion and the deposition time scales, namely,

$$\lambda = \frac{\tau_D}{\tau_R} = \frac{Kb}{D} \quad [22]$$

Thus, large values of  $\lambda$  mean that the deposition of particles on the cylinder walls is governed mainly by diffusion, whereas small values of  $\lambda$  mean that deposition is controlled by the local deposition rate.

An analytical solution of [13] (in its non-dimensional form) can readily be obtained for the case that  $U$  is independent of the radial coordinate  $r$ . Since  $U'$  and  $U''$  are indeed void of radial coordinate dependence for small particle radius to pore diameter ratios, we obtain after tedious manipulations,

$$P(\eta, \zeta, \tau) = \frac{1}{\sqrt{\pi\tau}} e^{-\frac{(\zeta - P_0\tau)^2}{4\tau}} \sum_{n=1}^{\infty} \left( \int_{\eta}^1 \eta J_0(\alpha_n \eta) d\eta \right) \frac{\alpha_n^2 J_0(\alpha_n \eta)}{(\lambda^2 + \alpha_n^2) J_0^2(\alpha_n)} e^{-\alpha_n^2 \tau} \quad [23]$$

where

$$\eta = \frac{r}{b} ; \quad \zeta = \frac{z}{b} ; \quad \tau = \frac{Dt}{b^2} \quad [24]$$

and  $J_0$  is the Bessel function of zero order.

The  $\alpha_n$  parameters are determined by the following indicial equation,

$$\alpha J_1(\alpha) = \lambda J_0(\alpha) \quad [25]$$

which has a countable number of roots  $\alpha_n$  ( $n=1,2,\dots$ ).

The expression for the probability distribution  $P$  in equation [23] is independent of the initial azimuthal angle  $\theta_0$  and radial position  $r_0$ . This is achieved by assuming that all initial positions of the particle at the pore entrance are equally probable and integrating the conditional probability distribution  $p$  over all these positions. Thus, [23] does not represent a solution for [13] it is rather the analytical solution for the physically plausible case based on  $p$ ,

$$P(\eta, \zeta, \tau) = b^3 \iint_{\Lambda_0} p(\eta, \zeta, \theta, \tau | \eta_0, 0, \theta_0) P(\eta_0, \theta_0) dA \quad [26]$$



where  $A_0 = \pi R_0^2$  is the cross-section area of the pore and  $P(\eta_0, \theta_0) = 1/A_0$  is the uniform probability distribution of finding a particle at time  $t=0$  at any arbitrary location at the pore entrance. It is interesting to note that  $P$  is independent of  $\theta$  due to the inherent axial symmetry of the problem.

Equations [23] and [25] can now be utilized to numerically compute more physically meaningful probabilities. For example, if we are to inquire what is the probability per unit length that a particle have deposited over the pore walls, a very long time after it have been introduced into the system, we simply calculate,

$$P_d(\zeta; P_e, \lambda) = - \int_0^{\infty} \left[ \frac{\partial P}{\partial \eta} \right]_{\eta=1} d\tau = \lambda \int_0^{\infty} [P]_{\eta=1} d\tau \quad [27]$$

where the right hand side equality stems from boundary condition [16]. It is easy to show that

$$P_d(\zeta; P_e, \lambda) = 4\lambda \sum_{n=1}^{\infty} \left( \int_0^1 \eta J_0(\alpha_n \eta) d\eta \right) \frac{\alpha_n^2}{(\lambda^2 + \alpha_n^2) J_0(\alpha_n) \sqrt{P_e^2 + 4\alpha_n^2} (\sqrt{P_e^2 + 4\alpha_n^2} - P_e)} \quad [28]$$

Figure 3 illustrates the numerically computed values of  $P_d$  as a function of  $z$  for Peclet numbers 1 and 10 and  $\lambda$  values 0.1, 0.5 and 1. The trend is very clear. High values of  $\lambda$  cause the probability density to decay very fast with  $z$ . This means that most of the particles would deposit on the walls very close to the pore entrance and deep penetration cannot be achieved. Figure 4 illustrates  $P_d$  as a function of Peclet number  $P_e$  for  $\lambda$  values 0.1, 0.5 and 1 and for given pore depths ( $z=0$  and  $1$ ). It manifests the very important role of particle convection. The probability density drops significantly with the Peclet number  $P_e$  thus a more even distribution of particles is expected along the pore axis and deeper penetration is expected. In figure 5 the probability density is directly plotted vs. the local deposition parameter  $\lambda$  for Peclet values 0.1, 1.0 and 10 and two values of  $z$ , showing again the fast accumulation of particles near the pore entrance for small values of Peclet number.

Figures 6 to 9 illustrate the foregoing conclusions vividly. Based on the probability density  $P_d$  we can define a new cumulative probability

$$P_c = \int_0^{z/b} P_d d\zeta \quad [29]$$

which can physically be interpreted as the long time ratio between the number of particles deposited over the pore walls up till pore depth  $z/b$  and the total number of particles introduced at  $z=0$  and  $t=0$ . The figures elucidate the fact that deep penetration (more than hundred pore diameters) can be achieved only for very low deposition parameters  $\lambda$  ( $\lambda < 0.1$ ) and for very high Peclet numbers ( $Pe > 100$ ). Cases in which  $\lambda = 0$  would obviously result in the deepest penetration. It might be achieved by introducing a repelling force between the particles and the pore walls, stronger than van der Waals forces. The asymptotic value of the cumulative probability for large values of  $z$  is always unity, since after a long time the probability that a particle has been deposited anywhere over the pore walls is unity (the particle cannot disappear).

Figure 10 summarizes the foregoing results. We define the penetration depth as the  $z/b$  value for which  $P_c = 0.9$ . In other words, 10 percent of the particles would penetrate deeper than the value shown in the figure for a given set of parameters, the local deposition rate  $\lambda$  and the Peclet number  $Pe$ . Obviously, the 0.9 numerical value chosen for  $P_c$  is quite arbitrary and a lower or a higher percentage could have been chosen. The basic interpretation of the results, however, would remain unaltered. It is obvious from figure 10 that the penetration depth for a given value of  $\lambda$  grows almost linearly with the Peclet number (which is not at all surprising). The slope of the curves depends strongly on  $\lambda$ : the smaller the  $\lambda$  value the deeper the particle penetration.

#### 4. CONCLUSIONS

- a) Deep penetration and coating is feasible by electrophoretic processes.
- b) Enhanced penetration is obtained for large electrophoretic Peclet numbers and small deposition rate constants.

- c) Electroosmosis increases Peclet number and thus penetration.
- d) The diffusion coefficient of the colloidal particles has a dual effect:
  - 1) decreasing diffusion coefficient causes increasing Peclet number which has a favorable effect on penetration depth.
  - 2) decreasing diffusion coefficient causes increasing deposition rate which has an unfavorable effect on penetration depth.
- e) The process can be controlled by a judicious selection of particle size and concentration, solution properties, electric field intensity and its time protocol.

acknowledgement

Research sponsored by the Air-Force Office of Scientific Research, Air-Force Systems Command, U.S.A.F. under Grant No AFOSR 89-0974. The U.S. Government is authorized to reproduce and distribute reprints for Governmental purposes notwithstanding any copyright notation thereon

## REFERENCES

1. F. Christin, R. Naslain and C. Bernard, *Proc. 7th Int. Conf. CVD* (T. O. Sedwick and H. Lydtin eds.) pp. 499-514 (1979).
2. F. Christin, L. Heraud, J.J. Choury, R. Naslain and P. Hagenmuller, *Proc. 3rd European CVD Conf.*, Neuchatel (1980).
3. F.A. Morrison, *J. Coll. Interface Sci.*, **34**, 210 (1970).
4. R.W. O'Brein and L.R. White, *J. Chem. Soc. Faraday II*, **74**, 1607 (1978).
5. A. Delgado, F. Gonzalez-Caballero and G. Pardo, *J. Non-Equilibrium Therm.*, **10**, 251 (1985).
6. C.F. Zukoski and D.A. Saville, *J. Coll. Interface Sci.*, **115**, 422 (1987).
7. R. Natarajan and R.S. Schechter, *AIChE J.*, **33**, 1110 (1987).
8. R.W. O'Brein, *J. Coll. Interface Sci.*, **92**, 204 (1983).
9. R.W. O'Brein and R.J. Hunter, *Can. J. Chem.*, **59**, 1878 (1981).
10. T. Okubo, *J. Coll. Interface Sci.*, **125**, 380 (1988).
11. R.W. O'Brein and D.N. Ward, *J. Coll. Interface Sci.*, **121**, 402 (1988).
12. L. Benguigui and I.J. Lin, *Electrostatics*, **21**, 205 (1988).
13. J.G. Harfield and R.C. Bunker, *Filtration and Separation*, **25**, 412 (1988).
14. M.C. Fair and J.L. Anderson, *J. Coll. Interface Sci.*, **127**, 388 (1989).
15. M.W. Kozak and J. Davis, *J. Coll. Interface Sci.*, **127**, 497 (1989).
16. F.A. Morrison and J.J. Stukel, *J. Coll. Interface Sci.*, **33**, 88 (1970).
17. H.J. Keh and J.L. Anderson, *J. Fluid Mech.*, **153**, 417 (1985).
18. N.G. van Kampen, *Stochastic Processes in Physics and Chemistry*, North-Holland (1983).
19. J. Happel, *Trans. N.Y. Acad. Sci.*, **20**, 404 (1958).
20. B. Gal-Or and S. Waslo, *Chem. Eng. Sci.*, **64**, 1431 (1968).
21. S. Kuwabara, *J. Phys. Soc. Japan*, **14**, 527 (1959).
22. D. Edwards, M. Shapiro and H. Brenner, *Phys. Fluids A*, **2**, 45 (1990).
23. A.A. Zick and G.M. Homsy, *J. Fluid Mech.*, **115**, 13 (1982).
24. A.S. Sangani and A. Acrivos, *Int. J. Multiphase Flow*, **8**, 343 (1982).
25. J.P. Sorensen and W.E. Stewart, *Chem. Eng. Sci.*, **29**, 819 (1974).
26. L.J. Snyder and W.E. Stewart, *AIChE J.*, **12**, 167 (1966).
27. A.J. Karabelas, T.H. Wegener and T.J. Hanratty, *Chem. Eng. Sci.*, **28**, 673 (1973).
28. S. Haber, *Electroosmosis in Porous Media* (submitted) (1990).

29. J. Happel and H. Brenner, *Low Reynolds Number Hydrodynamics*, Noordhoff (1973).
30. M.E. O'Neill, *Mathematica*, **11**, 67 (1964).
31. G. Hetsroni, S. Haber and E. Wacholder, *J. Fluid Mech.*, **41**, 689 (1970).
32. S.L. Goren, *J. Fluid Mech.*, **41**, 619 (1970).
33. S. Haber and R. Mauri, *J. Fluid Mech.*, **190**, 201 (1988).
34. R. Mauri and S. Haber, *SIAM*, **46**, 49 (1986).
35. L.H. Dill and H. Brenner, *PhysicoChem. Hydrodynam.*, **3**, 267 (1982).
36. S. Haber and H. Brenner, in *Recent Developments in Structural Continua*, edited by P.N. Kaloni and D. Dekee, Longman/Wiley, N.Y. (1986).
37. I. Frankel and H. Brenner, *J. Fluid Mech.*, **204**, 97 (1989).
38. M.W. Kozak and J. Davis, *J. Coll. Interface Sci.*, **112**, 403 (1986).
39. M. Shapiro and H. Brenner, *J. Aerosol Sci.*, **21**, 97 (1990).
40. M.E. O'Neill and S.R. Majumdar, *Z. Angew. Math. Phys.*, **21**, 164 (1970).
41. M.E. O'Neill and S.R. Majumdar, *Z. Angew. Math. Phys.*, **21**, 180 (1970).

figure captions

- fig. 1: A ~~slab~~<sup>model</sup> of a porous substrate of thickness  $c$ .
- fig. 2: The definition of the coordinate system and the geometrical model for particle penetration .
- fig. 3: The probability density  $P_d$  vs. the downstream nondimensional distance  $z/b$ .
- fig. 4: The probability density  $P_d$  vs. the electrophoretic Peclet number.
- fig. 5: The probability density  $P_d$  vs. the local ~~density~~<sup>deposition</sup> number.
- figs. 6-9: The cumulative probability  $P_c$  vs. the downstream nondimensional distance  $z/b$ .
- fig. 10: Penetration depth defined as the downstream value distance  $z/b$  for which there is 90 percent probability that the particle has deposited after a very long time vs the electrophoretic Peclet number (the local deposition number used as a parameter).

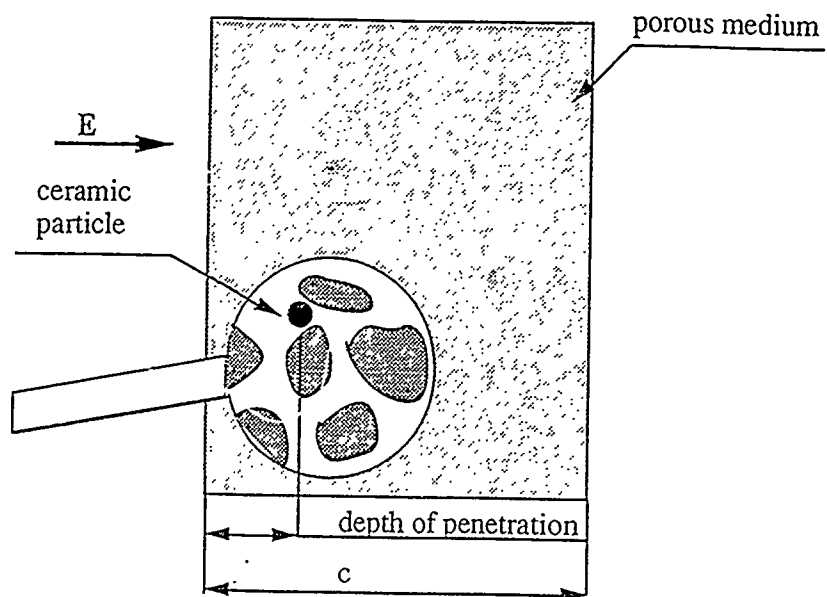


Fig.1

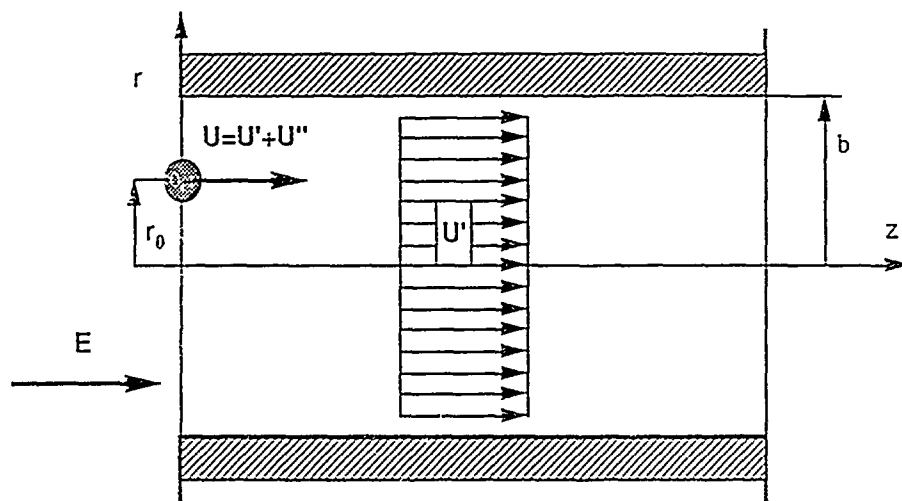


Fig.2



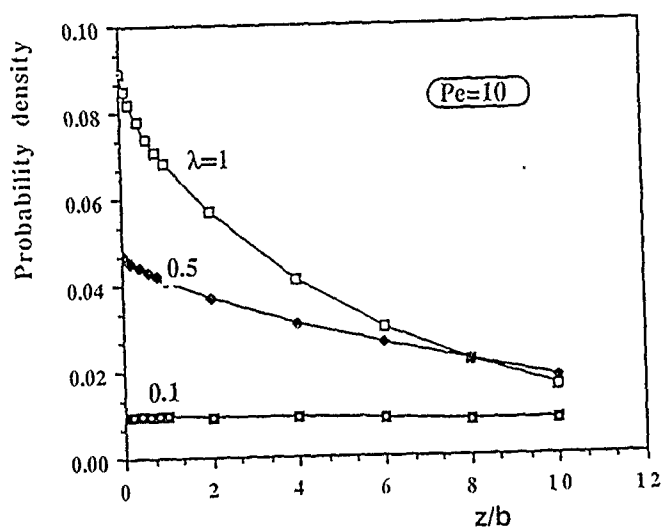
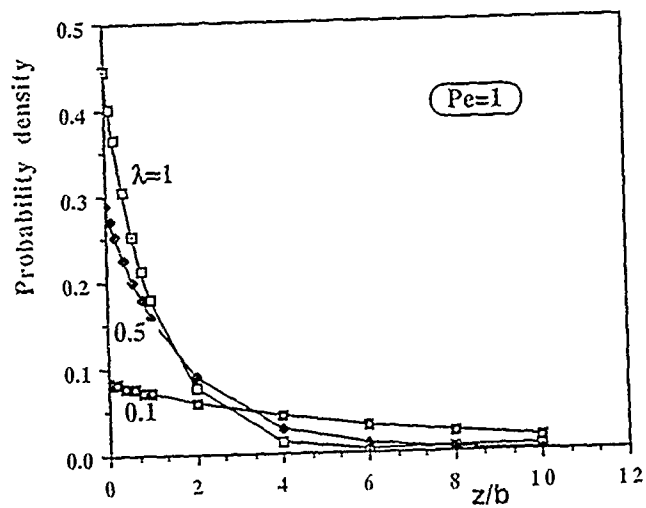


Fig.3

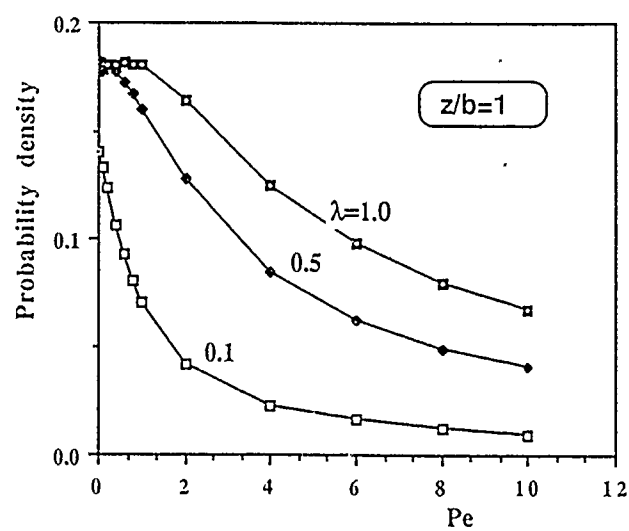
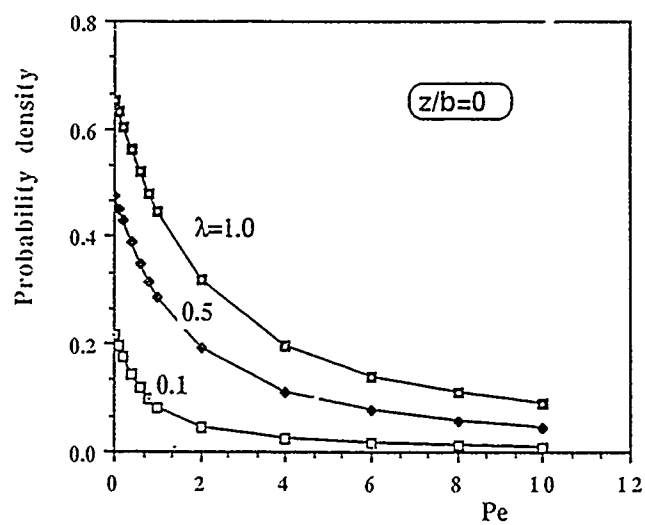


Fig.4

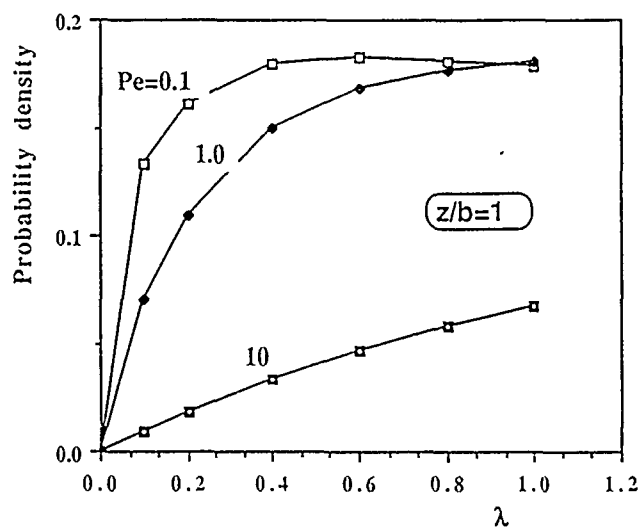
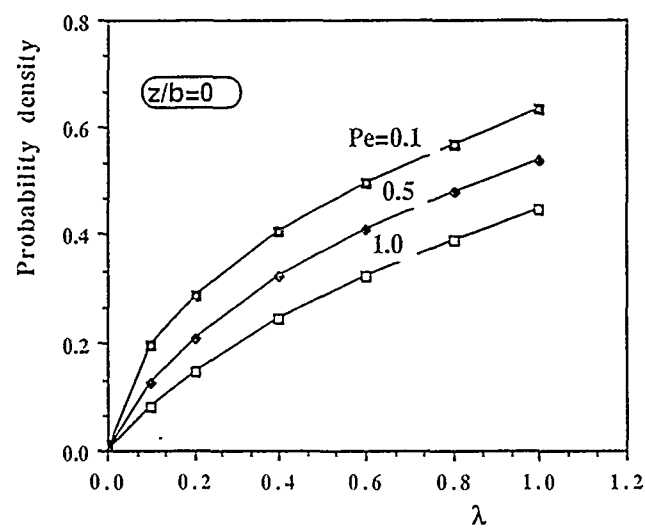


Fig.5

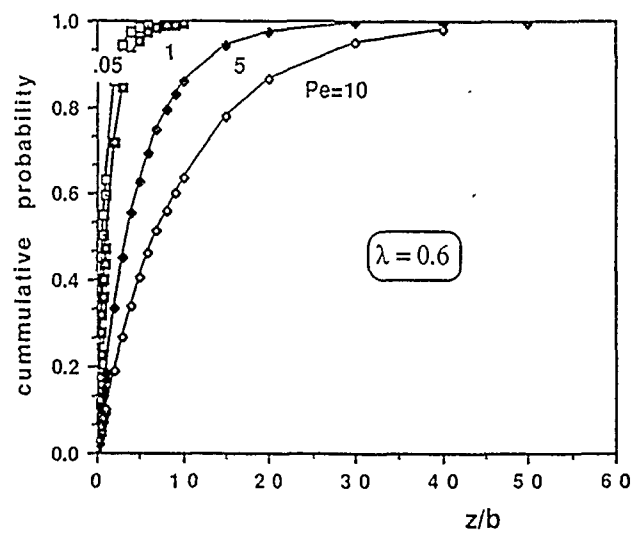
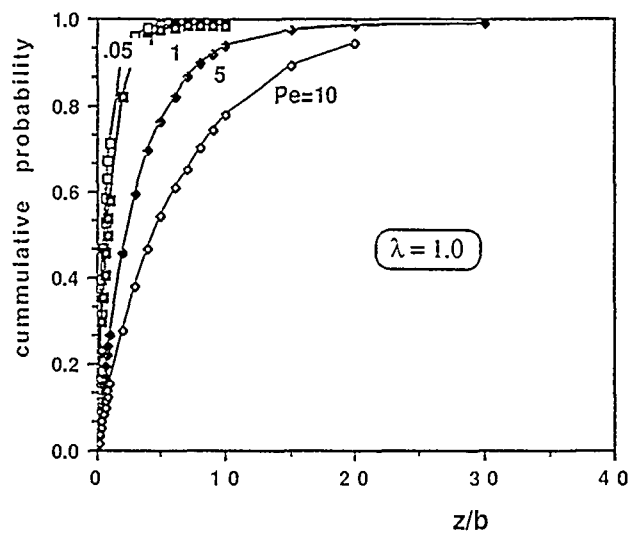


Fig.6

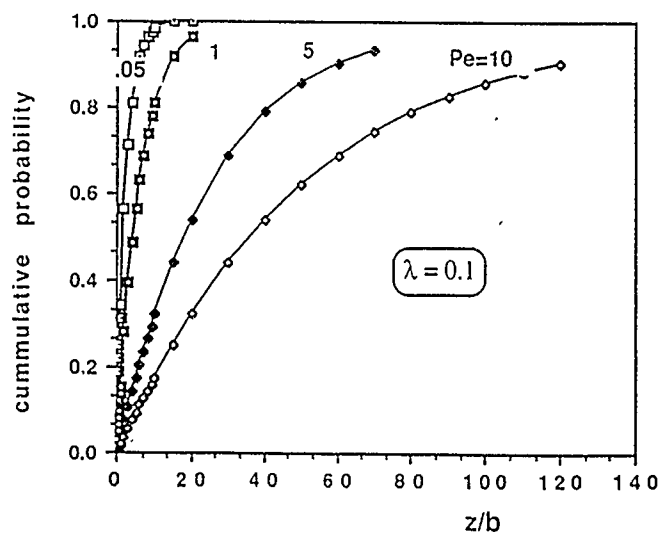
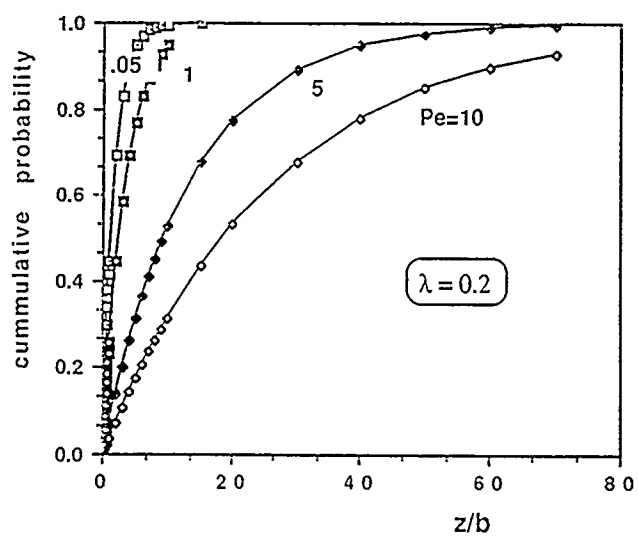


Fig.7

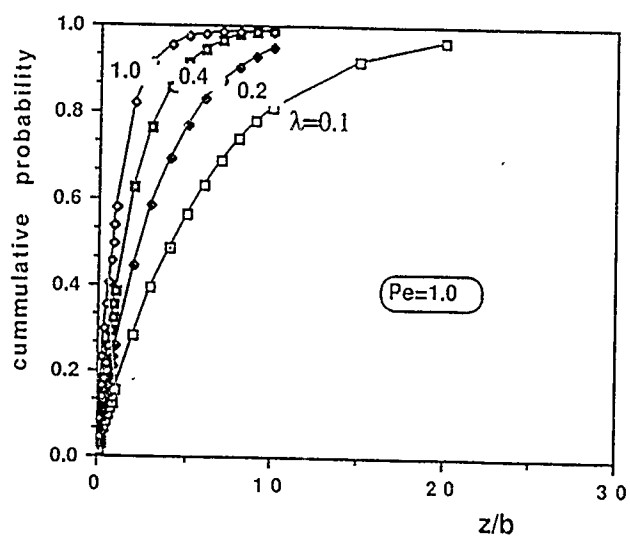
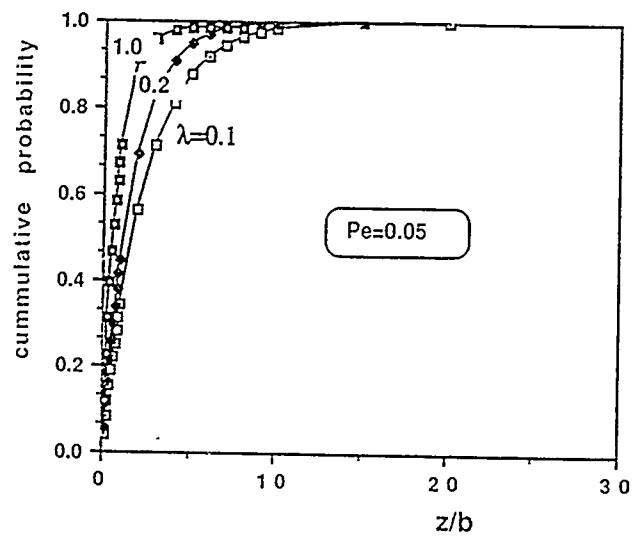


Fig.8

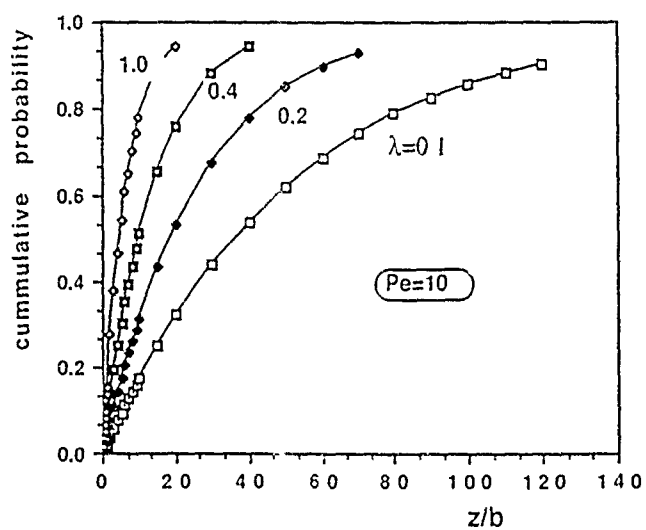
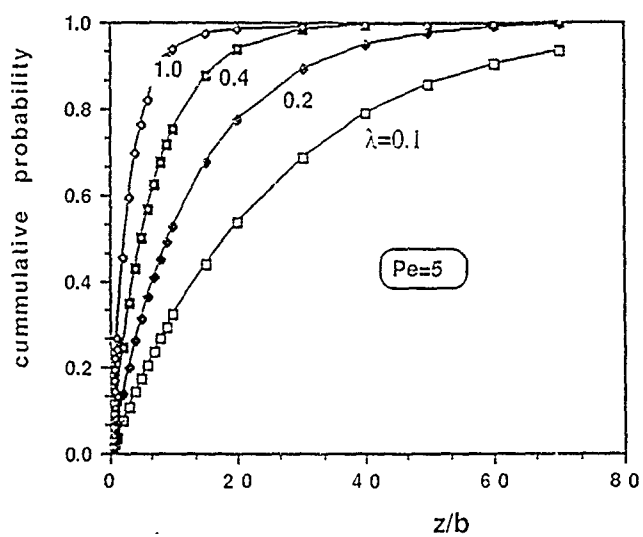


Fig.9

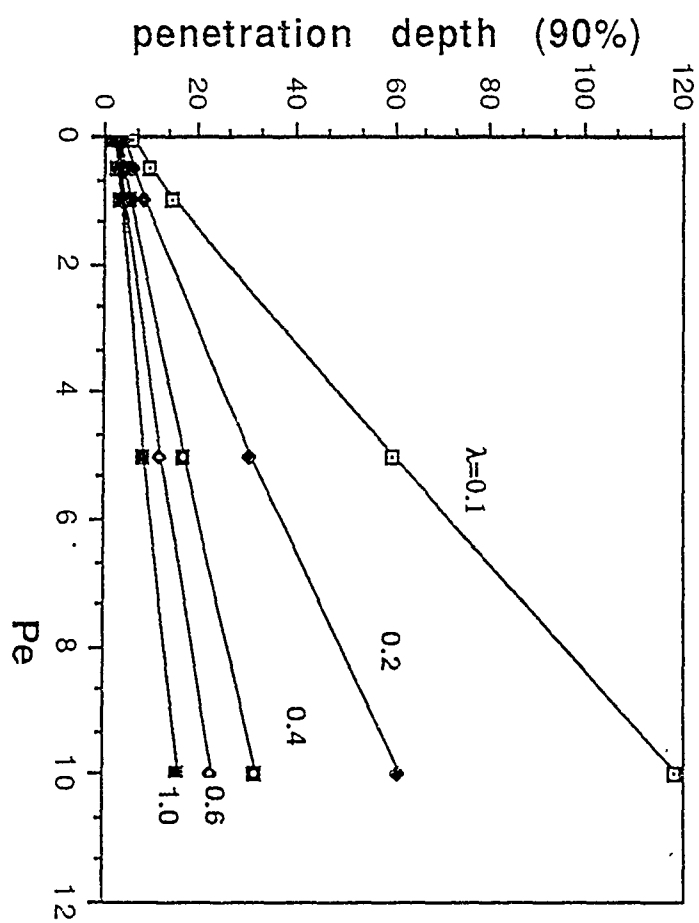


Fig.10



## Electrolytic $\text{ZrO}_2$ Coatings: I. Electrochemical Aspects

L. Gal-Or, I. Silberman\* and R. Chaim\*

Israel Institute of Metals

and

\*Department of Materials Engineering

Technion - Israel Institute of Technology

Haifa, 32000, Israel

### Abstract

$\text{ZrO}_2$  coatings were deposited on graphite and titanium from an aqueous solution in a two-step reaction: hydroxyl ions ( $\text{OH}^-$ ) were generated at the cathodic substrate by reduction of  $\text{NO}_3^-$  and dissolved  $\text{O}_2$ , and then reacted with zirconyl ions in the solution to form the hydroxide  $\text{Zr}(\text{OH})_4$ , which in turn decomposed on drying to yield zirconia ( $\text{ZrO}_2$ ).

A faradaic efficiency of 40-80% was found, attributable to reduction reactions that do not produce hydroxyl ions (such as reduction of  $\text{H}^+$ ), as well as to formation of the hydroxide at sites removed from the cathodic substrate. The effects of current density, time and hydrodynamic conditions on coating weight, cell voltage, temperature and pH of the solution were studied.

### Introduction

Ceramic coatings are currently of much interest for applications in high-temperature and severely corrosive environments. A variety of methods are available for their production, including plasma spraying [1,2], chemical vapor deposition and sputtering [3], and sol-gel processes [3-5].

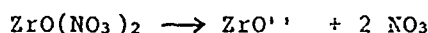
Formation of ceramic coatings by electrochemical means is a relatively new technique and has been described by Switzer [6] in application to synthesis of ceramic films and powders. It presents several advantages over alternative coating techniques: the thickness and morphology of the deposit can be controlled by the electrochemical parameters; relatively uniform deposits are obtainable on complex shapes; the deposition rate is higher than for most other

methods, and the equipment is of low cost [7].

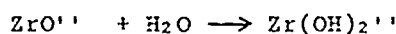
Electrodeposition has been used extensively for many years for production of metallic coatings. Later, oxides and hydroxides [6-9] were deposited by a redox change reaction induced on the anode. Formation of a ceramic oxide through cathodic reactions was demonstrated only recently by Switzer [6] with  $\text{CeO}_2$  coatings.

In the present work, deposition of zirconia ( $\text{ZrO}_2$ ) from an aqueous solution of zirconyl nitrate ( $\text{ZrO}(\text{NO}_3)_2$ ) was studied. The sequence of reactions leading to oxide formation is expected to be the following:

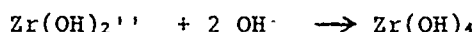
a) dissociation of the zirconyl salt :



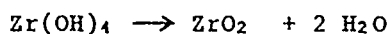
b) hydrolysis of the zirconyl ion :



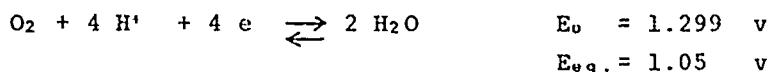
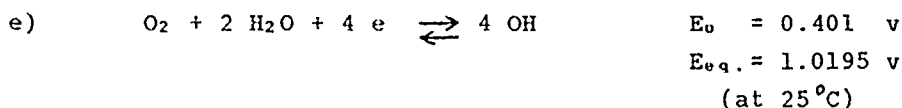
c) interaction of the hydrated cation with  $\text{OH}^-$  ions generated at the cathode by reduction reactions described further on:



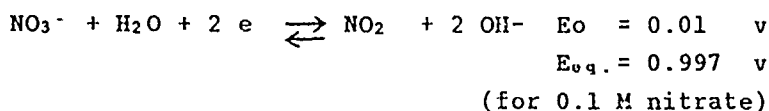
d) dehydration of the hydroxide :



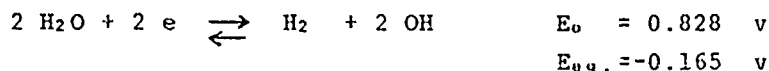
The cathodic reactions that generate  $\text{OH}^-$  and their standard and equilibrium potentials calculated with the aid of the Nernst equation are :



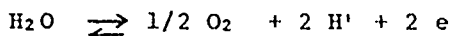
f) reduction of the  $\text{NO}_3^-$  ions :



g) reduction of  $\text{H}_2\text{O}$  :



The anodic reaction which occurs simultaneously is :



Thus, the hydroxide is formed in two successive steps : electrochemical generation of  $\text{OH}^-$ , and a chemical reaction

between the latter and the zirconyl cations. The deposit forms on the cathode, and a platinum electrode serves as anode.

The present paper describes the effects of the electrochemical deposition parameters on the formation rate of the  $ZrO_2$  coatings.

#### Experimental Procedure

The deposits were obtained on two different substrates, prepared in the form of 2 x 10 x 20 mm specimens : a) porous graphite (UC grade 45) and b) commercially pure titanium (ASTM B-265-58T). The graphite specimens were polished with a 1000 grit SiC abrasive paper, and the Ti plates machined and then polished with 180 grit paper. All specimens were then rinsed with ethanol in an ultrasonic bath, then washed with distilled water and dried in air.

The electrolyte used was a 0.1 M aqueous solution of  $ZrO(NO_3)_2 \cdot nH_2O$ , with an initial pH 2.3.

A power supply, Hipotronics 801-1A, was used, and cell voltage and current were measured with AVOmeters. Polarization curves were obtained with a PAR model 270 potentiostat. Deposits were obtained at current densities ranging from 15 to 100 mA/cm<sup>2</sup>, and durations of 10-60 minutes, in the course of which the cell voltage, and the pH and temperature of the solution were measured. Most experiments were performed without stirring, some with it.

The deposits were dried in air at room temperature. Coating weights were determined by weighing the specimens before and after deposition, within an accuracy of  $\pm 0.05$  mg. Some of the deposits were submitted to high-temperature treatments. Those on graphite were treated either at 900°C in argon or at 400 and 600°C in air, while those on Ti were treated at 780°C in air. The morphology and phase evolution of the deposits before and after the heat treatment were studied with the aid of scanning electron microscopy and x-ray diffraction, and reported in (10).

#### Results

The results described below refer only to the graphite specimens. Cathodic polarization curves are shown in Fig.1. For the unstirred solution, two polarization regions were

observed, representing reduction reaction associated with activation- and concentration-type polarization regimes respectively. Due to the range of the potentiostat (limited to -4 volt), the maximal current density (c.d.) achieved was limited to 55 mA/cm<sup>2</sup>, which prevented detection of a third cathodic reaction that must occur during deposition at higher c.d.'s.

The curve obtained for the stirred solution does not show domains of limited c.d., but the regions with different slopes indicate three cathodic reactions, which will be characterized and discussed later in detail.

The dependence of coating weight on the c.d. at which the coating was formed, for a constant deposition time of 60 min, is shown in fig.2. As could be expected, weight increases with current density, and the observed three modes of dependence apparently reflect the three cathodic reactions.

The dependence of coating weight on deposition time for two different c.d.'s is shown in fig.3. Coating weight increases with time in a decelerating manner. Stirring is seen to cause a significant reduction in the deposition rate (fig.4), by facilitating migration of OH<sup>-</sup> from the cathode into the bulk of the solution, so that the hydroxide formed does not accumulate on the cathode. The effect of stirring is weaker at high c.d.'s.

At high c.d.'s (above 75 mA/cm<sup>2</sup>), "strings" of gas bubbles were observed after a certain time, emerging from the surface of the coated substrate.

The deposition yield in terms of faradaic efficiency is relatively low and is presented in fig.5 as the actual coating weight compared with the theoretical weight, assuming that the electric charge served exclusively for generation of OH<sup>-</sup> ions.

The dependence of cell voltage on deposition time for different c.d.'s is shown in fig.6. The voltage is seen to increase with c.d. for a constant deposition time. At higher current densities, the voltage stabilizes at shorter times. This behavior is related to the mechanism of the coating formation and is discussed later.

The dependence of solution temperature on deposit and time is shown in fig.7, again for different c.d.'s. It is seen

that initially (for the first 10 min or so), the temperature level varies within a fairly narrow range, irrespective of the c.d. ; but in the longer run it rises drastically - the higher the c.d. , the steeper the rise. This thermal effect is due to the increase in electric resistance, following formation of the deposit.

The time pattern of the pH level of the solution is shown in fig.8 . Below 40 mA/cm<sup>2</sup> the pH hardly varied, but at higher c.d.'s significant changes were observed already from the outset. The explanation may be that the pH as measured was governed by the H<sup>+</sup> ions generated at the anode, since the OH<sup>-</sup> ions formed at the cathode were used up in deposit formation without contributing to the resultant pH of the bulk solution (see also below).

#### Discussion

In keeping with the electrochemical potentials of the various reduction reactions, the first reaction in the polarization curve is reduction of O<sub>2</sub> , with a relatively low limiting c.d. because of the low concentration of dissolved O<sub>2</sub> ; the second reaction is reduction of the NO<sub>3</sub><sup>-</sup> ions, and the third (unreflected in the polarization curve) is expected to be reduction of H<sup>+</sup> . Thus, while the first two reactions produce OH<sup>-</sup> ions, the third results in formation of H<sub>2</sub> .

With respect to coating weight as function of c.d. (fig.2), the first part of the curve (low c.d.'s of 0-15 mA/cm<sup>2</sup> ) is characterized by a relatively moderate (low deposition rate) slope (0.7 mg.cm<sup>2</sup> /mA), in turn associated with a low generation rate of OH<sup>-</sup> from reduction of O<sub>2</sub> (see fig.1). The steeper slope (of the order of 2.0 mg.cm<sup>2</sup> /mA) in the second part ( 15-75 mA/cm<sup>2</sup> ) represents a higher rate of deposit formation, associated with a high rate of OH<sup>-</sup> generation from the reduction of NO<sub>3</sub><sup>-</sup> . The third part ( 75-100 mA/cm<sup>2</sup> ) is again associated with a relatively moderate slope (0.7 mg.cm<sup>2</sup> /mA), due in this case to onset of reduction of H<sup>+</sup> ions to form H<sub>2</sub> , a reaction that does not produce OH<sup>-</sup> ions, hence does not contribute to deposit formation. As c.d. increases, more competitive electron-consuming reactions are activated.

The deviation of the actual coating efficiency from the

theoretical values may be due to the following phenomena :

- a) Charge transfer reactions that do not produce  $\text{OH}^-$  ions .
- b) Consumption of  $\text{OH}^-$  by  $\text{H}^+$  ions present in the original solution and generated at the anode.
- c) Undeposited  $\text{Zr}(\text{OH})_4$  formed in the bulk of the solution.

The increase in cell voltage with deposition time may be explained as follows :

In the initial stage of the coating process, the cathodic substrate is conductive and  $\text{OH}^-$  ions are generated over its entire surface. Due to the porosity of the substrate, a porous coating is initially formed. As the coating process progresses, the deposit becomes denser and thicker, and its electrical resistance increases, with the attendant increase in both cell voltage and solution temperature. The change in electric resistance is responsible in part for the accentuated limiting c.d.'s, and the relatively high potentials observed in the cathodic polarization curve of the unstirred solution (fig.1). After a certain time, the cell voltage reaches maximum, but the deposit continues to form while undergoing local breakdowns manifested in "strings" of gas bubbles. These breakdowns create sites of stronger reduction currents, which in turn enable the deposition process to continue, without further increase in the cell voltage. The deposit thus consists of two layers (see fig.1 in [10]); a thin dense layer formed in the first stage and a relatively thicker one formed in the second. The morphology of the deposit is in agreement with the proposed mechanism for formation of thick coatings.

The temperature increase may affect the diffusion rate of  $\text{OH}^-$  away from the cathode and that of  $\text{Zr}(\text{OH})_2$  toward it. Thus, it would be desirable to control the temperature during the coating experiments by stirring the solution; This, however would interfere with deposit accumulation on the cathode. Coating weight of nickel hydroxide was reported [11] to be unaffected by moderate agitation of the concentrated solution. In this regard, coating weight is expected to be influenced when low-concentration solutions and severe stirring conditions are used. It should be mentioned that the pH was measured in the bulk of the unstirred solution; local readings at the cathode may show an increase in pH due to the  $\text{OH}^-$  ions.

The present work demonstrated the outstanding potentialities of the electrolytic method for producing ceramic coatings, with relatively easy control of their thickness. However, it is necessary to control the drying stage in order to achieve sound and crack-free coatings. Optimal conditions for the formation of  $ZrO_2$  coatings are low current densities and short coating times, in view of the non-conductive nature of the oxide.

#### Acknowledgement

Research sponsored by the Air Force Office of Scientific Research, Air Force Systems Command, U.S.A.F., under Grant No. AFOSR 89-0474. The U.S. Government is authorized to reproduce and distribute reprints for Governmental purposes notwithstanding any copyright notation thereon.

#### References

- 1) T.E. Schmid and R.Y. Hecht, *Ceram.Eng.Sci.Proc.*, 9, 1089 (1988).
- 2) A. Kobayashi, N.Hasegawa and H. Namikawa, *Trans.J.W.R.I.* 18, 13 (1989).
- 3) M. Shane and M.L. Mecartney, *J.Mater.Sci.*, 25, 1537 (1990).
- 4) W.J. Dalzell and D.E. Clark, Dept. of Mater.Sci.Eng., Univ. of Florida, Gainesville, FL (1988).
- 5) D.E. Clark, W.J.Dalzell and D.C. Folz, *Ceram.Eng.Sci. Proc.*, 9, 1111 (1988).
- 6) J.A. Switzer, *Am.Ceram.Soc.Bull.*, 66, 1521 (1987).
- 7) G.E.F. Brewer, *Am.Ceram.Soc.Bull.*, 51, 216 (1972).
- 8) D. Tench and L. Warren, *J.Electrochem.Soc.*, 130, 869 (1983).
- 9) M. Sakai, T. Sekine and Y. Yamayaki, *J.Electrochem.Soc.* 130, 1631 (1983).
- 10) R. Chaim, I. Silberman and L. Gal-Or, this journal.
- 11) K.-C. Ho, *J.Electrochem.Soc.*, 134, 52 C (1987).

Figure Captions

Fig. 1 : Cathodic polarization curves for graphite in 0.1 M  $\text{ZrO}(\text{NO}_3)_2 \cdot n\text{H}_2\text{O}$  , at 2 mV/sec scan, stirred vs. unstirred solution.

Fig. 2 : Coating weight as function of current density for constant deposition time of 60 min.

Fig. 3 : Coating weight as function of deposition time for different current densities.

Fig. 4 : Coating weight as function of deposition time, stirred vs. unstirred solution.

Fig. 5 : Coating weight as function of electric charge.

Fig. 6 : Cell voltage as function of deposition time for different current densities.

Fig. 7 : Solution temperature as function of deposition time for different current densities.

Fig. 8 : pH of solution as function of deposition time for different current densities.



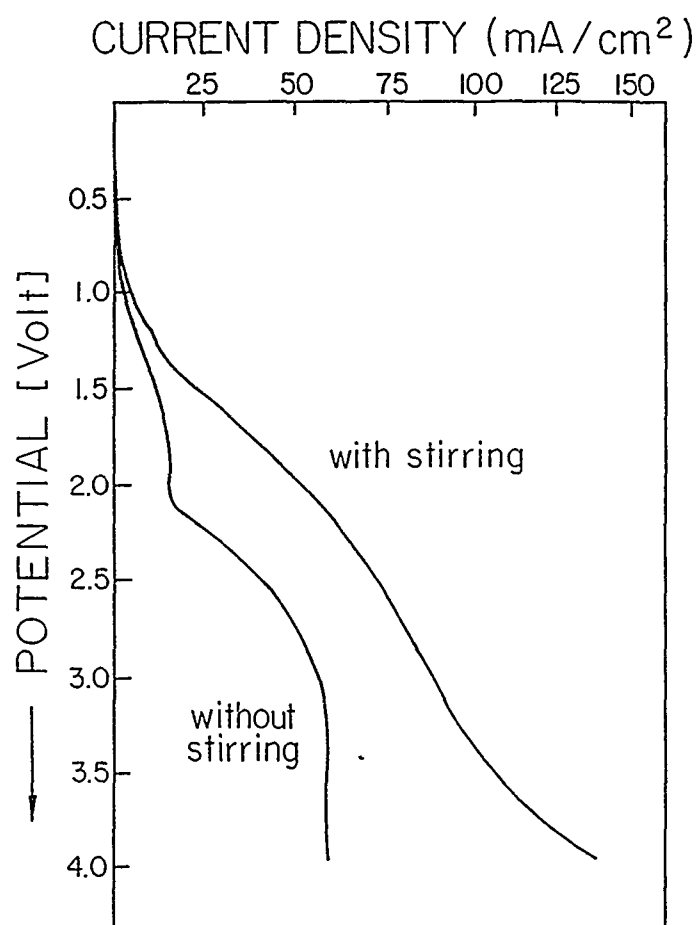


Fig. 1 : Cathodic polarization curves for graphite in 0.1 M  $\text{ZnO}(\text{NO}_3)_2 \cdot n\text{H}_2\text{O}$  , at 2 mV/sec scan, stirred vs. unstirred solution.

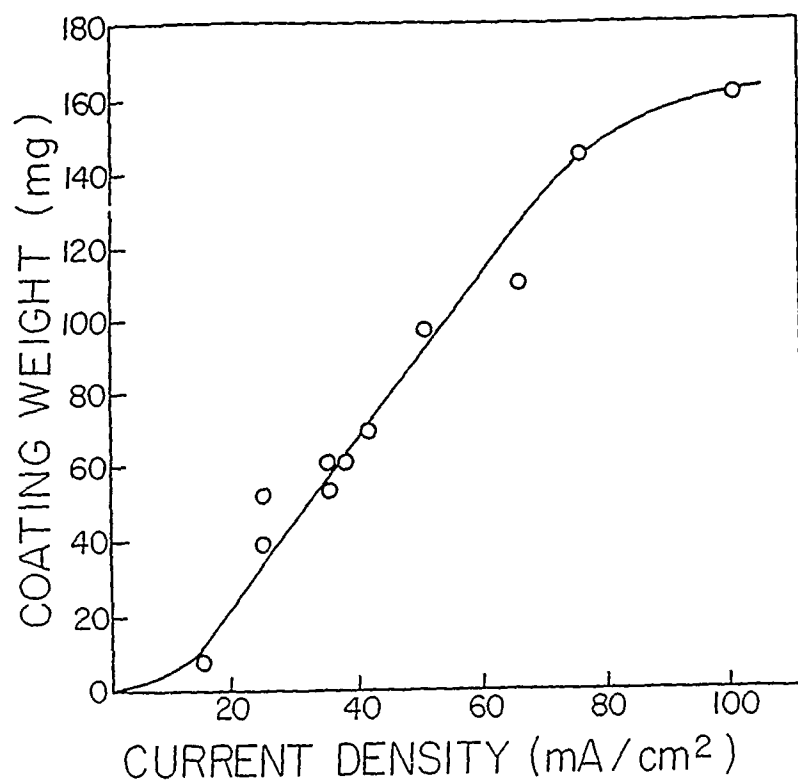


Fig. 2 : Coating weight as function of current density for constant deposition time of 60 min.

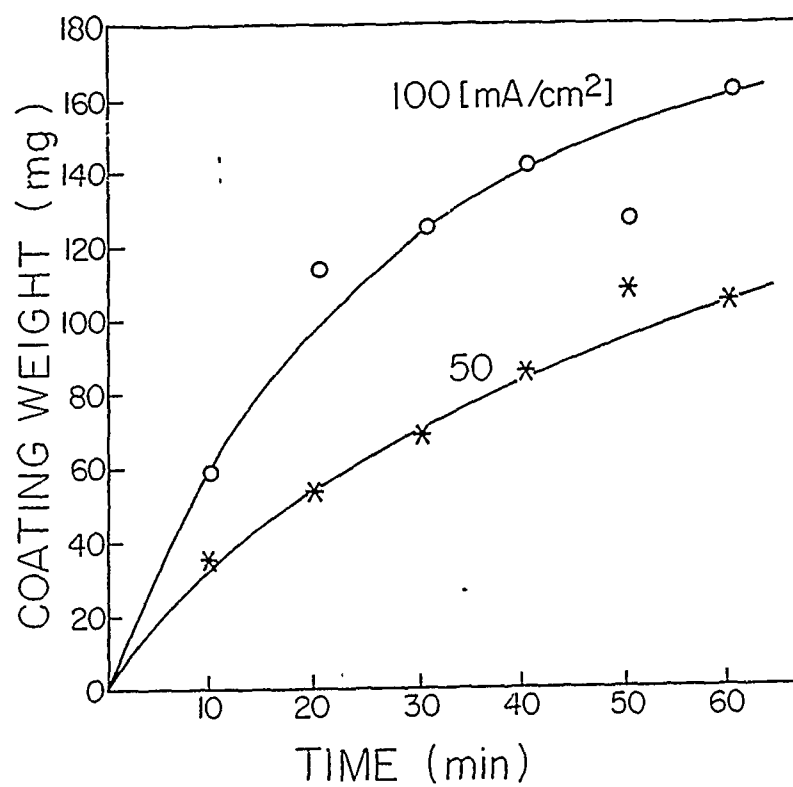


Fig. 3 : Coating weight as function of deposition time for different current densities.

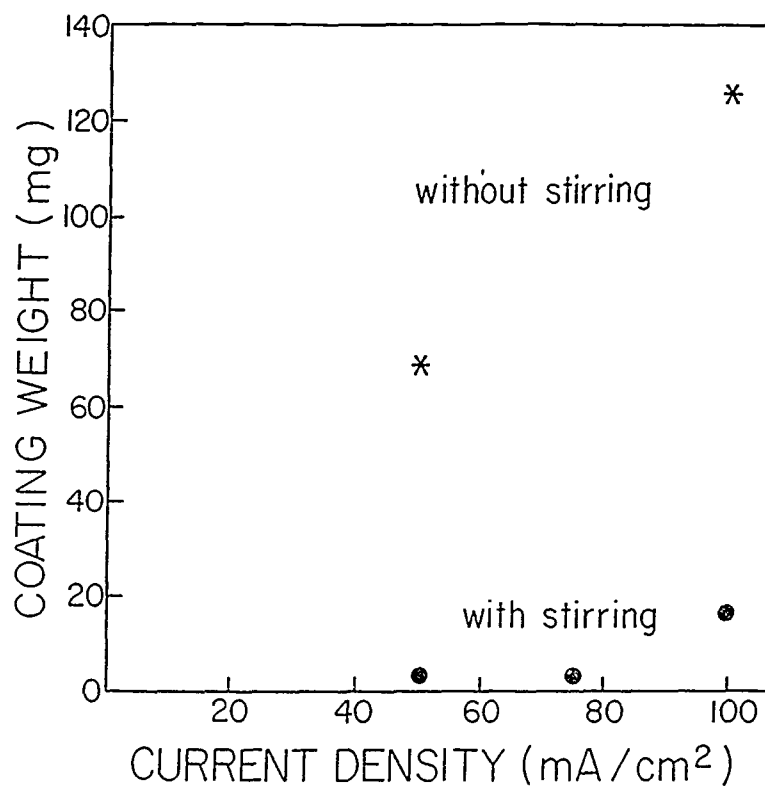


Fig. 4 : Coating weight as function of deposition time, stirred vs. unstirred solution.

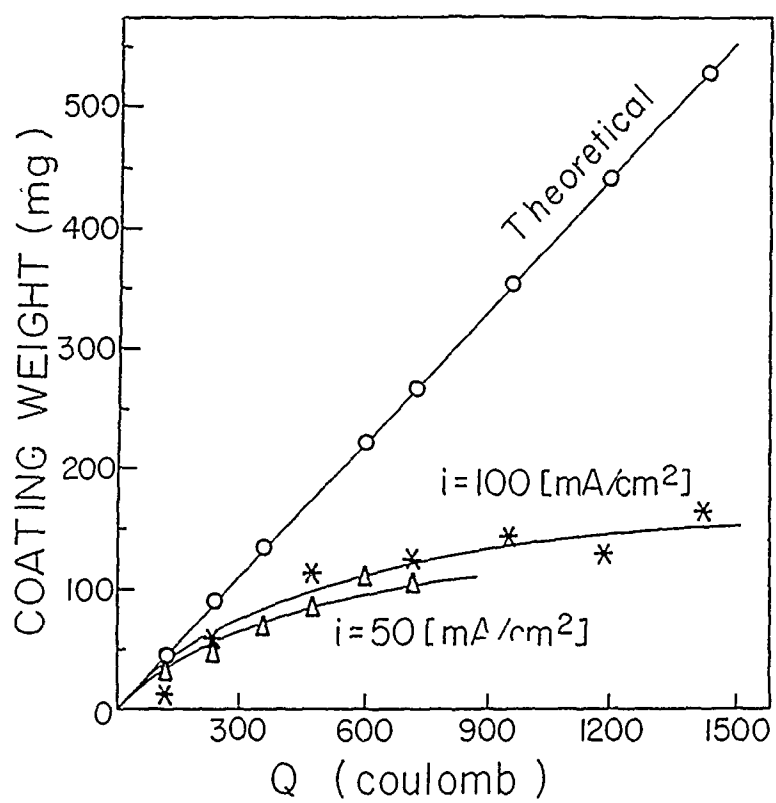


Fig. 5 : Coating weight as function of electric charge.

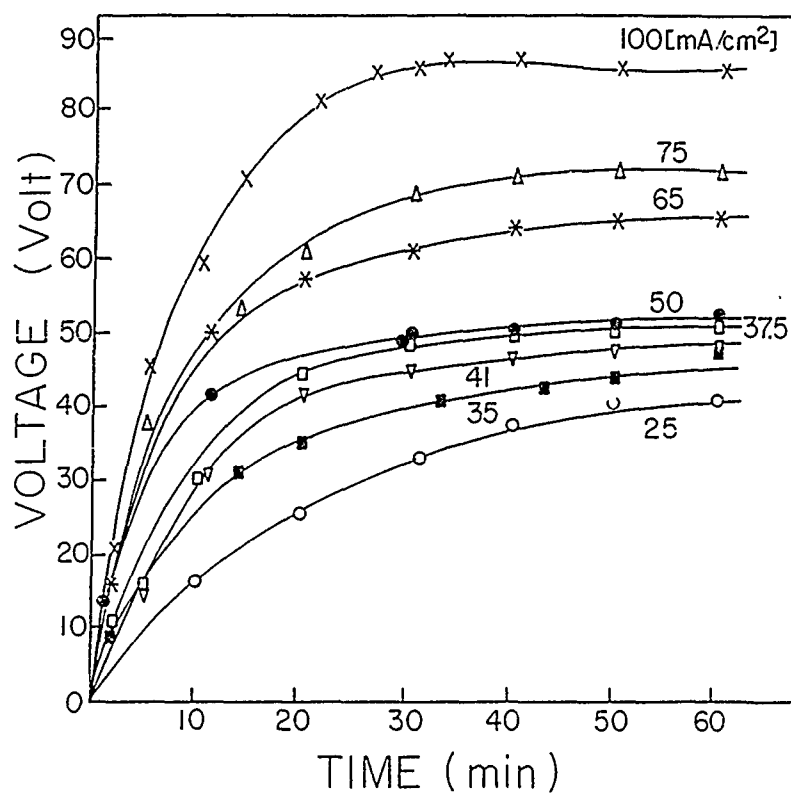


Fig. 6 : Cell voltage as function of deposition time for different current densities.

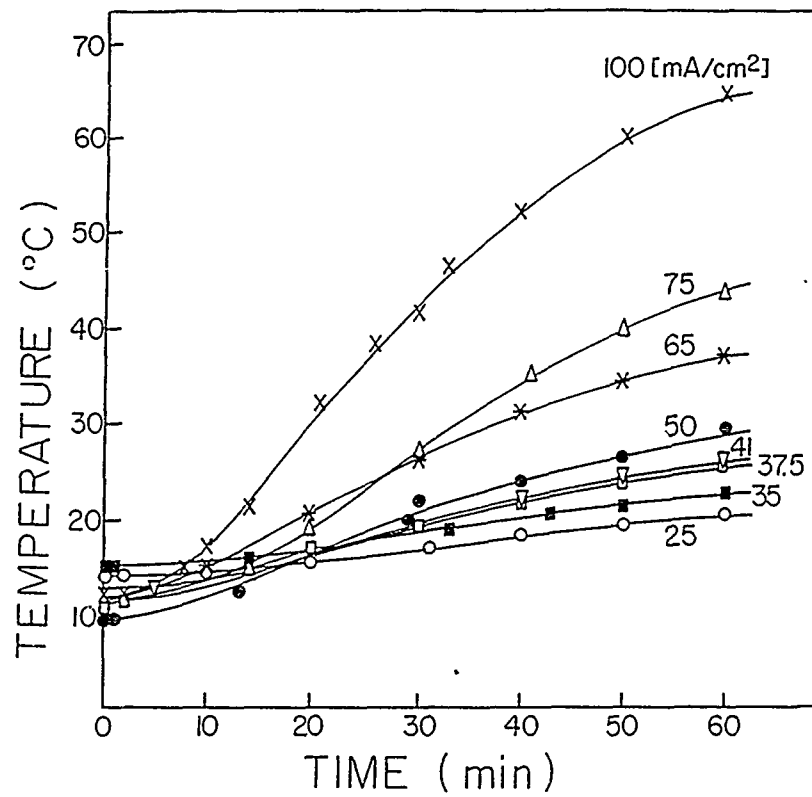


Fig. 7 : Solution temperature as function of deposition time for different current densities.

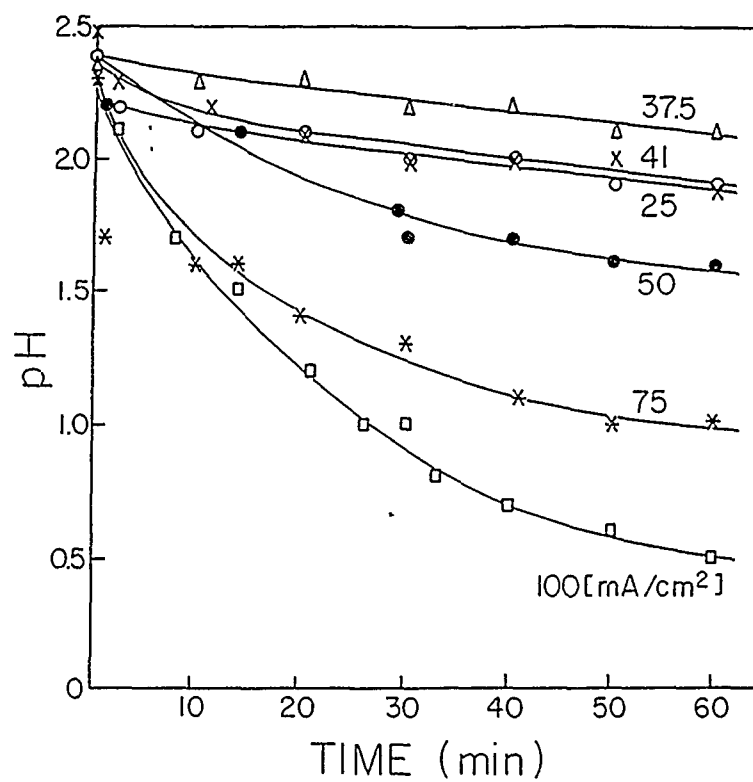


Fig. 8 : pH of solution as function of deposition time for different current densities.



## Electrolytic ZrO<sub>2</sub> Coatings : II. Microstructural Aspects

R. Chaim, I. Silberman and L. Gal-Or\*

Department of Materials Engineering  
and

\*Israel Institute of Metals  
Technion - Israel Institute of Technology  
Haifa, 32000, Israel

### Abstract

Zirconia coatings were formed on graphite and titanium substrates by electrodeposition. The as-deposited coatings were amorphous, and cracked during the drying stage. Sintering of the coatings on the graphite substrates caused crystallization, with formation of a variety of mixtures of the tetragonal and monoclinic ZrO<sub>2</sub> polymorphs, while oxidation of the Ti substrate and reaction with zirconia during the heat-treatment resulted in a microstructure resembling ceramic composite coatings.

### Introduction

Ceramic materials are finding ever wider application as thermal-barrier [1-2], wear-resistant [3-4], and corrosion-resistant [5-6] coatings.

The main ceramic coating methods fall into three categories : physical deposition, chemical deposition and reaction/conversion [7]. An electrochemical method also employed is based in on electrophoretic process in which the ceramic powder is suspended in a fluid, and deposited under the action of a high-strength electric field [8-11].

Recently, several workers used an electrochemical method to form coatings of transition-metal oxides and hydroxides [12], including thallium oxide [13-14], and cerium oxide [15] on metallic and semiconducting substrates directly from an aqueous solution. In such process, the microstructure and composition of the coating can be controlled by varying the

electrochemical parameters and the solution composition.

The present paper deals with the microstructural evolution of the electrolytically formed zirconia coatings on graphite and titanium substrates, as described in part I of this series [16].

#### Experimental procedure

The substrates chosen were 2 x 10 x 20 mm plates of commercial graphite (48 % porosity, average pore size of 60 micron) and commercially pure titanium (ASTM # B 265-58T) materials which differ in their chemical affinity to zirconia. The graphite was polished with 1000 grit SiC abrasive paper, while the titanium plates were surface-finished by machining. The plates were finally rinsed with ethanol and distilled water and then dried in air.

The electrolyte was a 0.1 M aqueous solution of zirconyl nitrate  $ZrO(NO_3)_2 \cdot nH_2O$ , with an initial pH adjusted to 2.3. A total surface area of  $\sim 4$  [cm<sup>2</sup>] of the substrate was immersed in the solution. Deposition was effected at current densities within the range of 15-100 [mA/cm<sup>2</sup>] and 10-60 minute durations. For a more detailed description of the deposition process see [16].

The deposits formed on the substrates were dried in air at room temperature. Firing was carried out at 400, 600°C in air, and 900°C in argon, for 1 hr for the graphite substrates, and at 780°C for 1 hr in air for the titanium.

The microstructure of the zirconia coatings was characterized during the different stages of the process, using optical and scanning electron microscopy (SEM) (Model JSM-840). The phase content was determined by X-ray diffraction with the diffractometer (Model PW-1730) operated at 40 KV and 40 mA, using monochromatized Cu k-alpha radiation, at a scanning speed of 0.4 [degree/min].

#### Results

The as-deposited ceramic coatings appeared as a transparent viscous fluid, especially at high current densities and long coating durations, where thick deposits were formed. In-situ microscopical observations of the drying process showed simultaneous development of cracks within the coating layer on graphite. The wet coating

deposit was characterized by a high content of bubbles. During drying some of the bubbles coalesced to form larger ones, while others were expelled from the deposit and migrated to its surface. The drying process was thus accompanied by formation of discontinuities within the coating, which converted into deep cracks towards the end of the drying process. The resultant coating layer had a "cracked-mud" appearance (as shown in figs.1 and 2) irrespective of the substrate material. The coating thickness was found to increase with both current density and coating duration. Thicker coatings showed larger islands in the cracked-mud morphology.

Thick coatings (over ~ 20 micron) on the graphite substrates often consisted of two layers, the upper layer being thicker and composed of coarser islands (fig.1b). Circular traces of the drying pools were also observed, especially at the centers of these coarse islands (fig.1c), but were almost absent in the coatings on the Ti substrates (fig.2b).

X-ray diffraction spectra of the dry as-deposited coatings and of the fired coatings are shown in figs.3 and 4 for the graphite and Ti substrates, respectively. The coating layers before firing have the typical spectrum of amorphous zirconia, in which a broadened amorphous-type peak appears around the angle  $2\theta \sim 30$  degrees (figs. 3a and 4a) irrespective of the substrate material. This finding is consistent with the relatively smooth and featureless morphology of the as-deposited coating surfaces (figs.1 and 2).

Firing induced a different phase evolution and morphology in these substrate/coating systems, and the resulting fired coatings were opaque. The microstructure of the coating on the graphite substrate was characterized by fine equiaxed submicron particles (fig.5). These particles were identified as a mixture of tetragonal and monoclinic polymorphs of zirconia (fig.3b), based on the  $\{111\}$  and  $\{400\}$ -type reflections. The broadening of the  $\{111\}$ -type reflections was used to calculate the crystallite size of the polymorphs with the aid of the Scherrer equation [17], while the volume fractions of the two phases were determined through the 'polymorph' equation as corrected by Porter and Heuer [18]. The crystallite size was found to be 2 and 12 [nm] for the

400°C and 600°C treatments respectively, with the polymorphs undistinguishable. By contrast, treatment at 900°C for 1 hr in argon resulted in distinct crystallite sizes of 25 and 20 [nm] for the tetragonal and monoclinic phases, with volume fractions of 15% and 85% , respectively. These size data indicate that the SEM image (fig. 5) represents zirconia aggregates.

The zirconia coating on the Ti substrates exhibited a totally different inner microstructure. Oxidation of the metallic titanium during firing resulted in the original spaces between the cracks in the coating layer being filled by the growing titanium oxide (fig.6). Microchemical EDS analyses of the various features of the coating (see Table I), and elemental mapping for Ti (fig.6d) confirmed the Ti-rich nature of the polycrystalline phase between the zirconia islands. An appropriate X-ray diffraction spectrum from this specimen (fig. 4b) contained reflections of  $\text{TiO}_2$  in the form of rutile,  $\text{ZrO}_2$  with the tetragonal and monoclinic phases, and additional reflections coincident with those of the  $\text{Zr}_{0.72}\text{Ti}_{0.28}\text{O}_{0.28}$  ,  $\text{Zr}_{0.5}\text{Ti}_{0.5}\text{O}_{0.33}$  ,  $\text{Zr}_{0.5}\text{Ti}_{0.5}\text{O}_{0.19}$  hexagonal phases [19]. The volume fractions of the tetragonal and monoclinic phases in these coatings were calculated to be 37% and 63% , and their crystallite sizes 26 and 25 [nm], respectively.

The surface microstructure was more complex and dependent on the coating layer thickness prior to firing. At locations with greater coating thicknesses (i.e. at the bottom of the machining grooves), titanium oxide growth was confirmed to the gaps between the zirconia islands (fig.6c). However, at locations with smaller coating thicknesses (i.e. top of the machining grooves), the oxide grew to extent that it partially buried the zirconia islands (fig.6e). In both cases, the centers of the islands appeared to have reacted with the titanium substrate (see also fig.9), and were most probably converted into the titanium zirconate phases. EDS results from such regions (Table I) have revealed compositions similar to those of titanium zirconate phases, which were identified by XRD (fig.4b).

In many cases, traces were observed on the titanium oxide layer parallel to the periphery of the zirconia islands (arrowed in fig.7). These traces could be identified as the

original contours of the zirconia prior to firing. By their means, the firing shrinkage of the coating was estimated to be of the order of ~20 %, assuming a similar percent shrinkage for the third dimension (the coating thickness).

The diamond Vickers microhardness of the coating on the Ti substrates has an average value of 520 [Kg/mm<sup>2</sup>]. Scratches were applied manually to the coating surface with a diamond indenter, in order to characterize qualitatively the adherence and brittleness of the composite coating layer. A typical trace of one of these scratches is shown in fig.8 ; it exhibits a high density of microcracks perpendicular to the scratch direction. The presence of these microcracks in the smeared region indicates heavy deformation of the material by the indenter. Moreover, some regions of the coating near the scratch trace were debonded from the substrate (fig.9). This debonding occurred by crack propagation either through the coating or at the substrate/coating interface. In the latter case, the fractured surface was composed of very fine dimples, indicating some ductility at the interface.

#### Discussion

The microstructural and morphological evolution within the coating layer may be explained in relation to the affinity of the substrate material to chemical reaction with the coating.

The electrochemical deposition, whereby zirconium hydroxide gel is precipitated from the solution at ambient temperature on the cathode, leads to the amorphous character of the coating.

The bubbles resulting from the drying process were observed only in coating layers formed on the graphite substrates. Consequently, the bubbles within the wet coatings may be related to the entrapped gases within that substrate, due to its porous nature. The non-porosity of the Ti substrates prevented such bubble formation. Still, the coatings in both systems showed surface microcracks after the drying stage. This type of morphological development is attributable to non-uniform contraction of the wet coating. Densification of the latter during the drying process results in tensile stresses within it, the level of these

stresses depending upon the mismatch in thermal expansion coefficient and elastic constants between the coating and substrate materials. While thicker coatings may withstand biaxial stresses in their plane better than thinner ones, stresses perpendicular to the coating/substrate interface are larger for thicker coatings, and may cause spalling. The resultant morphology is reflected in fewer cracks in the thicker coating layers, hence in formation of larger zirconia islands.

Firing of the zirconia coatings on graphite substrates at the various temperatures, led to crystallization of the amorphous coating. According to the Ellingham diagram [20], graphite oxidizes under these firing conditions to form CO gas, but no reaction with the zirconia is expected to occur. Low-temperature firing of amorphous zirconia was reported to produce low-temperature polymorphs [21-22]. The pH of the mother solution was also reported to affect the ratio of tetragonal/monoclinic phase contents after calcination at 400 to 600°C [23-24]. At low pH (less than about 5) a mixture of these low temperature polymorphs is expected to be formed, as was confirmed for the present coatings. Formation of undoped zirconia via solution by different techniques often results in a mixture of the polymorphs, their relative volume fractions depending upon crystallite size [25-26]. The crystallite size of the tetragonal polymorph present in the coating (12-25 nm) is also consistent with the reported particle-size range within which this phase is stable [21-22].

By contrast, firing of the coatings on Ti substrates has resulted in a more complex morphology, due both to oxidation of Ti and to its reaction with the coating. In this case the firing temperature was 780°C, at which Ti exhibits an oxidation regime of a parabolic type [27-28]. Under this regime, oxidation is said to occur by diffusion of Ti atoms towards the surface of the growing oxide layer. Thus, while the surface of the Ti substrate at the cracks is exposed to air and oxidation, the regions below the zirconia islands are subjected to relatively low oxygen partial pressures, assuming solid contact at the zirconia/Ti interfaces. Accordingly, at these interfaces, oxidation of Ti occurs by interdiffusion of Ti, Zr and oxygen. The titanium zirconate

phase, with its low oxygen stoichiometry, is evidence of this reaction.

It was found that the reaction between the Ti and the coating was limited to the centers of the zirconia islands, where significant volume contraction was observed. This effect is attributable to differential shrinkage of the islands during firing. Due to the temperature gradient across the zirconia layer, the islands are expected to bend upward at the edges during sintering, thus losing contact with the Ti substrate along their periphery. Furthermore, oxidation of Ti at 780°C occurs mainly by diffusion of Ti rather than that of oxygen through the growing oxide layer, a circumstance which favors formation of the low-oxygen titanium zirconate phase.

Finally, the qualitative scratch test of the coating and its debonding behavior indicate relatively good adhesion to the Ti substrate. In this regard, the chemical reactions between substrate, coating and atmosphere determine the microstructural evolution within the coating. The characteristic microstructure which resulted from these reactions suggests possibilities for formation of composite ceramic coatings.

#### Acknowledgment

Research sponsored by the Air Force Office of Scientific Research, Air Force Systems Command, USAF, under Grant No. AFOSR 89-0474. The US Government is authorized to reproduce and distribute reprints for governmental purposes notwithstanding any copyright notation thereon.

#### References

- 1) I. Zaplatynsky, Thin Solid Films, 95, 275 (1982)
- 2) R.J. Bratton and S.K. Lau, in "Advances in Ceramics" Vol.3, Science and Tech. of Zirconia, Eds. A.H. Heuer and L.W. Hobbs, p.226, ACS Pub., Columbus, Ohio (1981).
- 3) H.E. Hintermann, Wear, 100, 381 (1984).
- 4) J. Halling and R.D. Arnell, Wear, 100, 367 (1984).
- 5) J.W. Vogan, L. Hsu and A.R. Stetson, Thin Solid Films, 84, 75 (1981).
- 6) G. Perugini, Thin Solid Films, 108, 415 (1983).

- 7) T.E. Schmid and R.J. Hecht, *Ceram.Eng.Sci.Proc.*, 9, 1089 (1988).
- 8) G.E.F. Brewer, *Am.Ceram.Soc. Bull.*, 51, 216 (1972).
- 9) D.E. Clark, W.J. Dalzell and D.C. Folz, *Ceram.Eng.Sci. Proc.*, 9, 1111 (1988).
- 10) D.R. Brown and F.W. Salt, *J.Appl.Chem.*, 15, 40 (1965).
- 11) L. Gal-Or and S. Liubovich, Report AFOSR Grant No.88-0097, March (1989).
- 12) D. Tench and L. Warren, *J.Electrochem.Soc.*, 130, 869 (1983).
- 13) M. Sakai, T. Sekine and Y. Yamazaki, *J.Electrochem.Soc.* 130, 1631 (1983).
- 14) J.A. Switzer, *J.Electrochem.Soc.*, 133, 722 (1986).
- 15) J.A. Switzer, *Am.Ceram.Soc.Bull.*, 66, 1521 (1987).
- 16) L. Gal-Or, I. Silberman and R. Chaim, this journal.
- 17) E.D. Cullity, "Elements of X-Ray Diffraction", p.284, Addison-Wesley Pub. Co., Reading, Massachusetts (1978).
- 18) D.L. Porter and A.H. Heuer, *J.Am.Ceram.Soc.*, 62, 298 (1979).
- 19) L.E. Fykin, V.V. Vavilova, I.I. Kornilova, R.P. Ozerov, and S.P. Solov'iev, *Dokl.Phys.Chem.*, 194, 823 (1970).
- 20) L.S. Darken and R.W. Gurry, "Physical Chemistry of Metals", McGraw-Hill Book Co., N.Y. p.349 (1953).
- 21) E. Tani, M. Yoshimura and S. Somiya, *J.Am.Ceram.Soc.*, 66, 11 (1983).
- 22) P. Singh and S.K. Date, *J.Mater.Sci.Lett.*, 6, 621 (1987).
- 23) R.Srinivasan, R. De Angelis and B.H. Davis, *J.Mater.Res.* 1, 583 (1986).
- 24) S.S. Jada and N.G. Peletis, *J.Mater.Sci.Lett.*, 8, 243 (1989).
- 25) R.G. Garvie, *J.Phys.Chem.*, 69, 1238 (1965).
- 26) M.V. Swain, *J.Mater.Sci.Lett.*, 5, 1159 (1986).
- 27) P.H. Morton and W.M. Baldwin, *Trans.ASM*, 44, 1004 (1952).
- 28) P. Kofstad, K.Hauffe and H. Ljollesdal, *Acta Chem.Scand.* 12, 239 (1958).



Table I : EDS composition results for ceramic coating on Ti substrates.\*

Microstructural feature	Chemical composition (mole%)		Remarks**
	Zr	Ti	
Zirconia island center (reacted regions)	48.0	52.0	P1 in fig.6e
	59.0	41.0	
	65.0	35.0	
	69.0	31.0	
	76.0	24.0	
Zirconia island periphery (non-reacted regions)	73.0	27.0	P2 in fig.6e
	85.0	15.0	
	87.0	13.0	
Oxidized regions between zirconia islands	9.0	91.0	P3 in fig.6e
	0.0	100.0	
	0.0	100.0	

\* Fired at 780°C for 1 hr in air.

\*\* Examples for the analyzed regions.

Figure Captions

Fig. 1 : SEM images of dried zirconia coatings on graphite resemble a "cracked-mud" morphology both for (a) thin coating (25 mA/cm<sup>2</sup> for 15 min) and (b) thick coating (25 mA/cm<sup>2</sup> for 75 min). Thick coatings (i.e. 100 mA/cm<sup>2</sup> for 60 min) are often composed of two layers, with the upper layer containing drying pools (arrowed in (c)). (d) Cross-section shows penetration of the coating into pores of the graphite.

Fig. 2 : SEM images of dried zirconia coatings on Ti showing the "cracked-mud" morphology. This featureless surface morphology is characteristic of the amorphous nature of the coating. (b) At higher magnifications, no drying pools are visible in coatings on Ti.

Fig. 3 : X-ray diffraction spectra of zirconia coatings on graphite. (a) Amorphous-type broadened peak from the as-deposited coating and the sharp peak from the graphite (gr) substrate. (b) Reflections from the tetragonal (t) and monoclinic (m) polymorphs are characteristic of the ZrO<sub>2</sub> coatings, sintered at 600°C for 1 hr.

Fig. 4 : X-ray diffraction spectra of zirconia coatings on Ti . (a) Absence of sharp reflections from a deposited coating indicates on its amorphous nature. (b) Typical reflections from alpha-Ti, TiO<sub>2</sub> (rutile-R), ZrO<sub>2</sub> (tetragonal-t and monoclinic-m ) and various zirconium titanates (ZT) are seen for coatings sintered at 780°C for 1 hr.

Fig. 5 : SEM image of sintered (600°C/ 1 hr) zirconia coating on graphite. The submicron particles represent aggregates constituting a mixture of tetragonal and monoclinic polymorphs of zirconia.

Fig. 6 : SEM images of sintered zirconia coatings on Ti, showing formation of  $\text{TiO}_2$  at the cracks between the zirconia islands. (a) At low and (b) higher magnifications, the topography of the machining grooves is visible. (c) At the bottom of grooves "BG", the  $\text{TiO}_2$  crystals grew only between the zirconia islands. (d) Ti elemental mapping of (c). (e) At the top of grooves "TG",  $\text{TiO}_2$  crystals grow and bury the zirconia islands (see text for further details).

Fig. 7 : SEM image showing the line traces of the zirconia island contours prior to (arrowed) and after sintering, from which the sintering shrinkage may be deduced.

Fig. 8 : SEM image of the scratch trace, showing high density of microcracks at the smeared regions, perpendicular to the scratch direction.

Fig. 9 : SEM images showing: (a) Typical coating cross-section where fine  $\text{TiO}_2$  crystals grew around the zirconia islands, accompanied by shrinkage and bending. (b) Debonding at the coating/substrate interface results in dimpled fracture surfaces.

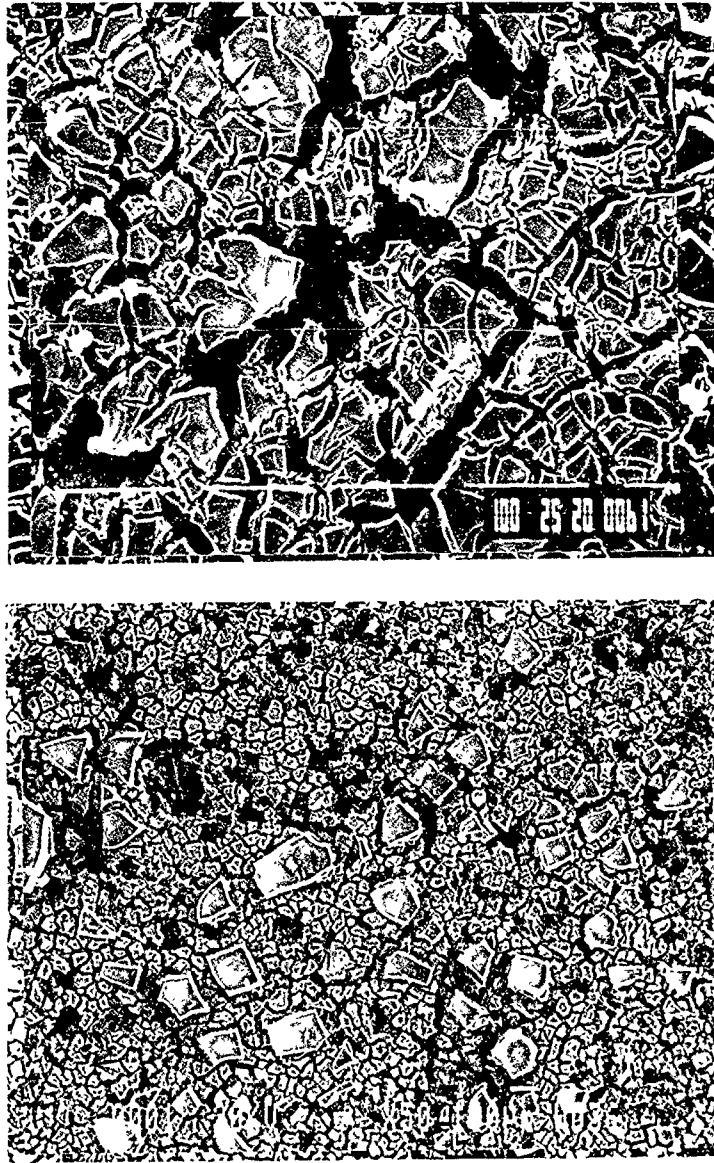


Fig. 1 : SEM images of dried zirconia coatings on graphite resemble a "cracked-mud" morphology both for (a) thin coating ( $25 \text{ mA/cm}^2$  for 15 min) and (b) thick coating ( $25 \text{ mA/cm}^2$  for 75 min). Thick coatings (i.e.  $100 \text{ mA/cm}^2$  for 60 min) are often composed of two layers, and the upper layer containing drying pools (arrowed in (c)). (d) Cross-section shows penetration of the coating into pores of the graphite.

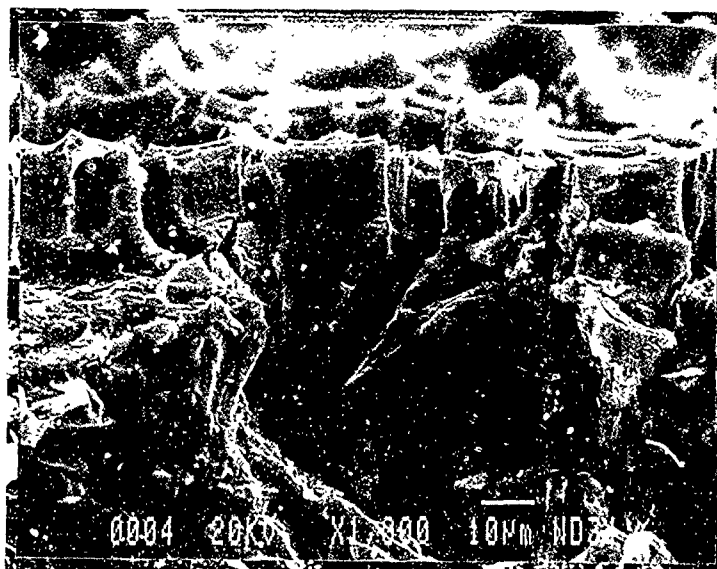


Fig. 1



Fig. 2 : SEM images of dried zirconia coatings on Ti showing the "cracked-mud" morphology. This featureless surface morphology is characteristic of the amorphous nature of the coating. (b) At higher magnifications, no drying pools are visible in coatings on Ti.

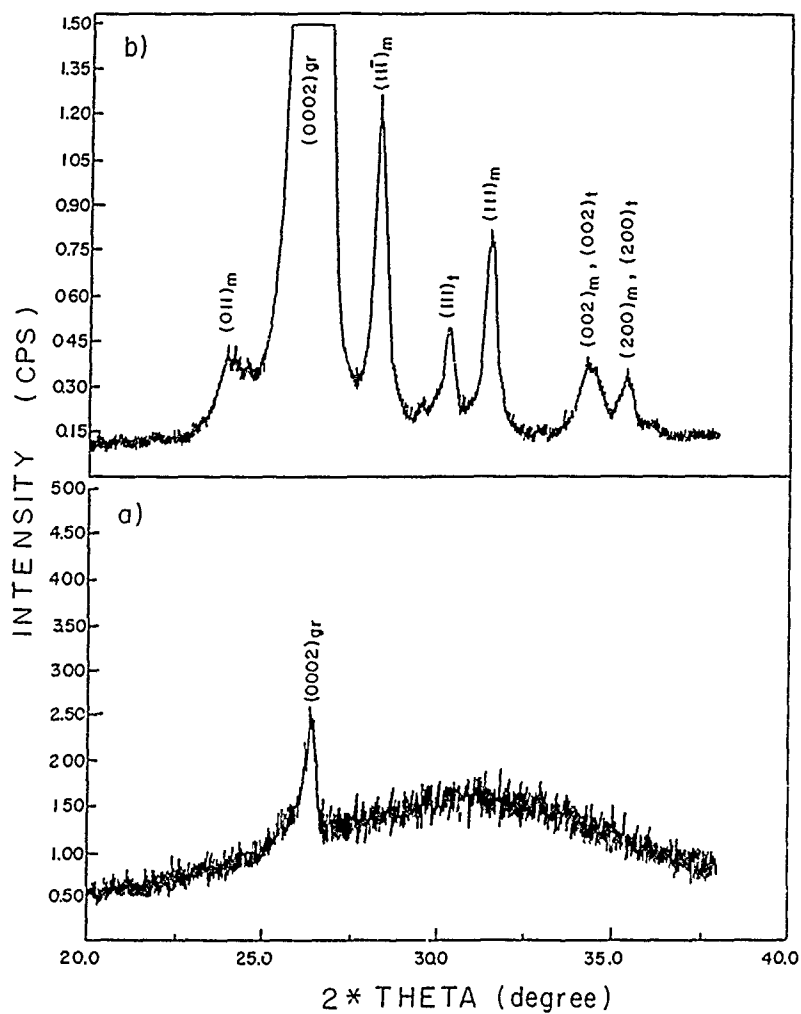


Fig. 3 : X-ray diffraction spectra of zirconia coatings on graphite. (a) Amorphous-type broadened peak from the as-deposited coating and the sharp peak from the graphite (gr) substrate. (b) Reflections from the tetragonal (t) and monoclinic (m) polymorphs are characteristic of the  $\text{ZrO}_2$  coatings, sintered at  $600^\circ\text{C}$  for 1 hr.

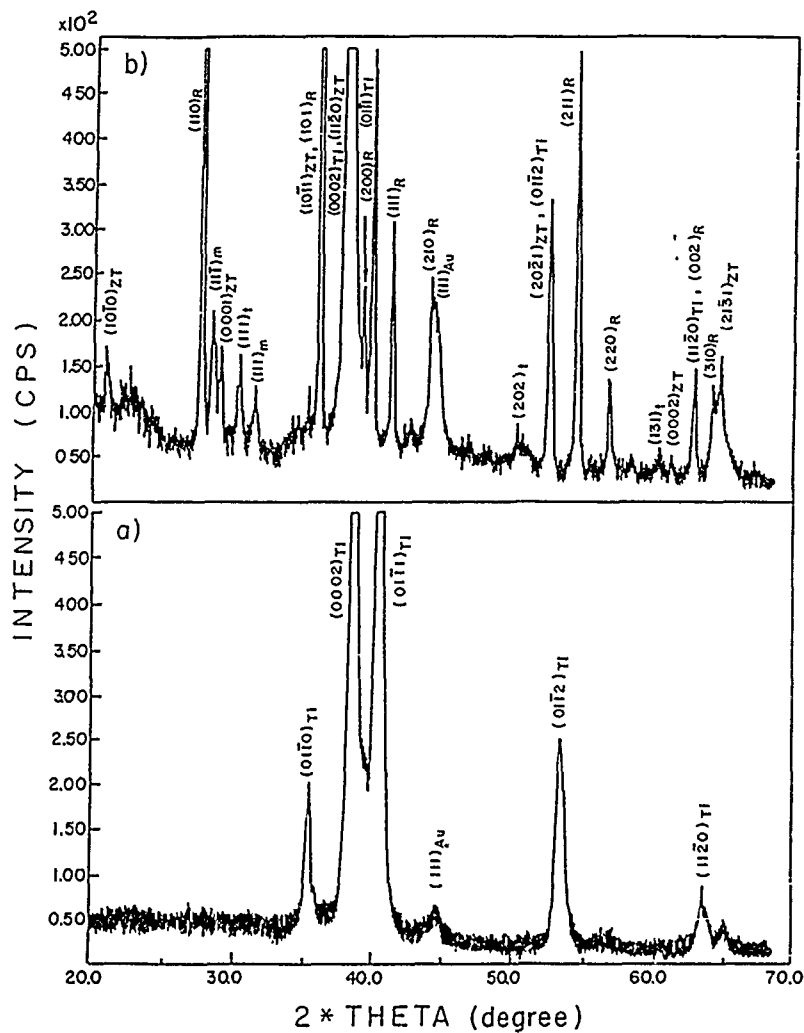


Fig. 4 : X-ray diffraction spectra of zirconia coatings on Ti . (a) Absence of sharp reflections from a deposited coating indicates on its amorphous nature. (b) Typical reflections from alpha-Ti,  $TiO_2$  (rutile-R),  $ZrO_2$  (tetragonal-t and monoclinic-m ) and various zirconium titanates (ZT) are seen for coatings sintered at  $780^\circ C$  for 1 hr.





Fig. 5 : SEM image of sintered ( $600^{\circ}\text{C}/1\text{ hr}$ ) zirconia coating on graphite. The submicron particles represent aggregates constituting a mixture of tetragonal and monoclinic polymorphs of zirconia.

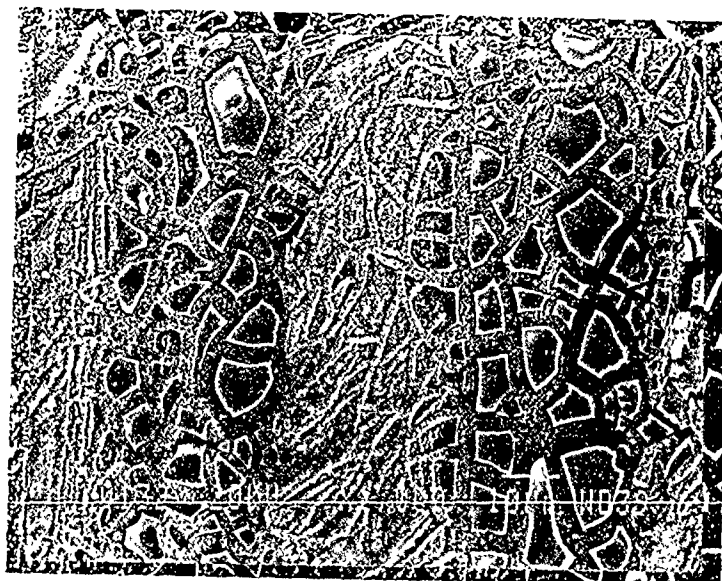
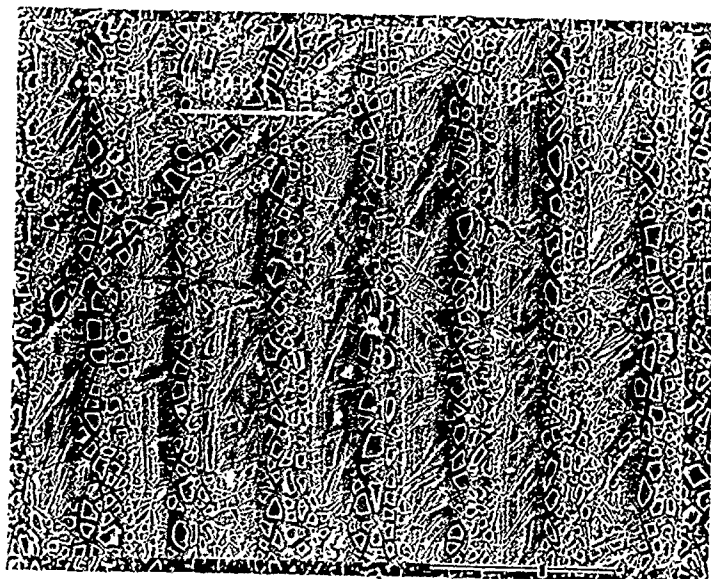


Fig. 6 : SEM images of sintered zirconia coatings on Ti, showing formation of  $\text{TiO}_2$  at the cracks between the zirconia islands. (a) At low and (b) higher magnifications, the topography of the machining grooves is visible. (c) At the bottom of grooves "BG", the  $\text{TiO}_2$  crystals grew only between the zirconia islands. (d) Ti elemental mapping of (c). (e) At the top of grooves "TG",  $\text{TiO}_2$  crystals grow and bury the zirconia islands (see text for further details).

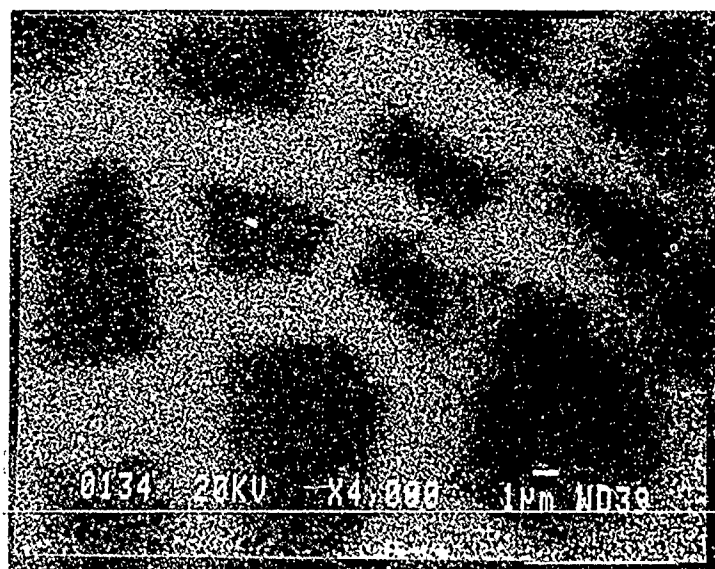
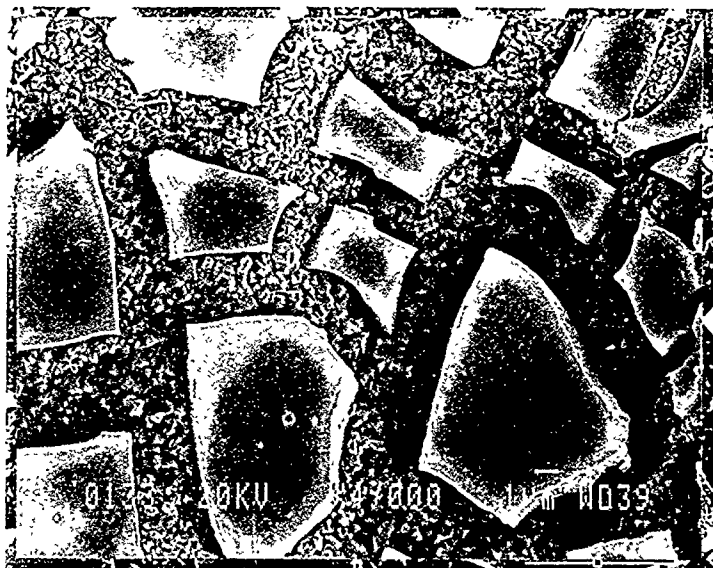


Fig. 6



Fig. 6



Fig. 7 : SEM image showing the line traces of the zirconia island contours prior to (arrowed) and after sintering, from which the sintering shrinkage may be deduced.

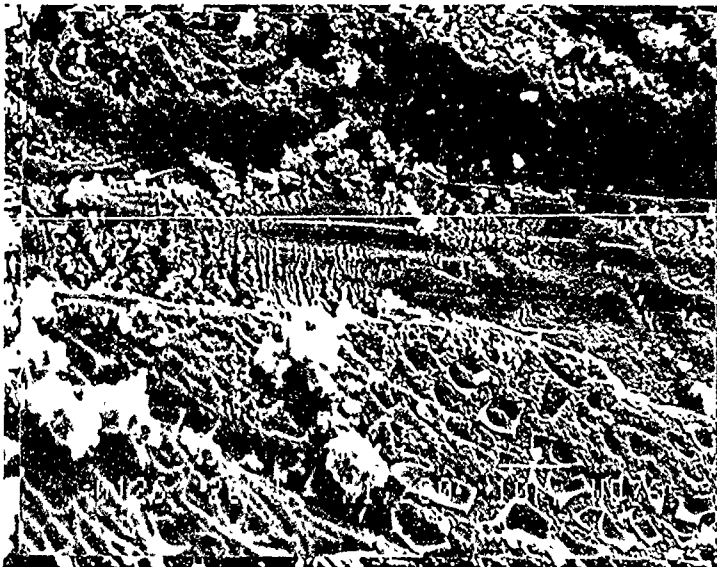


Fig. 8 : SEM image of the scratch trace, showing high density of microcracks at the smeared regions, perpendicular to the scratch direction.

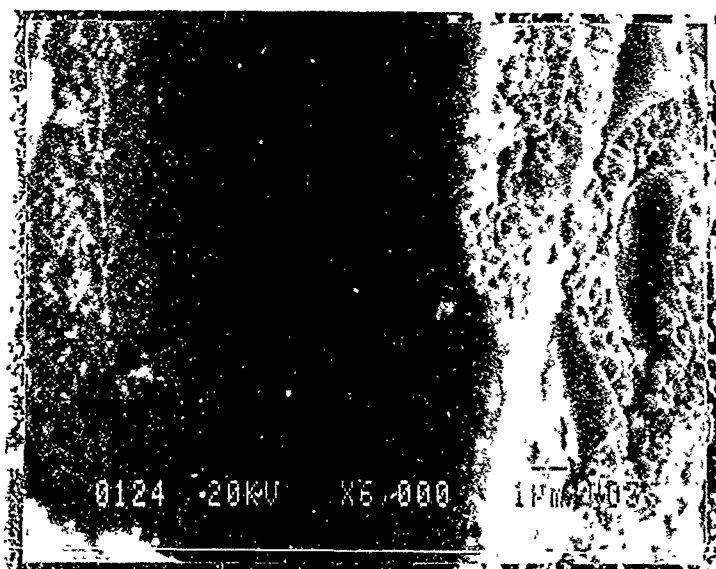
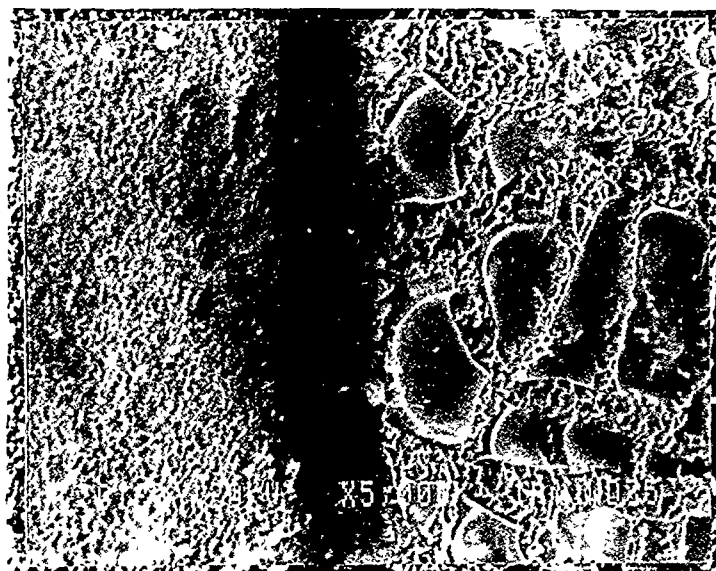


Fig. 9 : SEM images showing: (a) Typical coating cross-section where fine  $\text{TiO}_2$  crystals grew around the zirconia islands, accompanied by shrinkage and bending. (b) Debonding at the coating/substrate interface results in dimpled fracture surfaces.